Momentum Governors of California Undercurrent Transport

Ru Chen, James C. Mcwilliams, Lionel Renault

Momentum Governors of California Undercurrent Transport

RU CHEN,[a] JAMES C. MCWILLIAMS,[b] AND LIONEL RENAULT[c,b]

[a] *School of Marine Science and Technology, Tianjin University, Tianjin, China*
[b] *Department of Atmospheric and Oceanic Sciences, University of California, Los Angeles, Los Angeles, California*
[c] *LEGOS, University of Toulouse, IRD, CNRS, CNES, UPS, Toulouse, France*

(Manuscript received 26 September 2020, in final form 22 June 2021)

ABSTRACT: The California Undercurrent (CUC) transport, with significant variability ranging from weeks to decades, has consequences for both the climate and biogeochemistry of the California Current system. This study evaluates the governors of the CUC transport and its temporal variability from a momentum perspective, using a mesoscale-resolving regional model. From a 16-yr mean perspective, the along-isobath pressure gradient acts to accelerate the CUC, whereas eddy advection retards it. The topographic form stress, which is part of the volume integrated along-isobath pressure gradient, not only acts in the direction of the time-mean CUC, but also greatly modulates the temporal variability of the CUC transport. This temporal variability is also correlated with the eddy momentum advection. The eddy stress plays a role in transferring both the equatorward wind stress and poleward CUC momentum downward. A theory is formulated to show that, in addition to the conventional vertical redistribution of momentum, the eddy stress can also redistribute momentum horizontally in the area where the correlation between the pressure anomaly and isopycnal fluctuations has large spatial variability.

KEYWORDS: Ocean; Coastal flows; Eddies; Momentum; Topographic effects; Regional models

1. Introduction

The poleward-flowing California Undercurrent (CUC) on the continental slope off North America is an important part of the California Current system (e.g., Gay and Chereskin 2009). The CUC transports the relatively warm, salty, hypoxic, and nutrient-rich equatorial water in the alongshore direction from the equatorial Pacific to Vancouver Island (e.g., Hickey 1979; Garfield et al. 1999). It also plays a significant role in the regional hydrographic and biogeochemical balances, hence climate and productivity as well (e.g., Pierce et al. 2000; Thomson and Krassovski 2010; Meinvielle and Johnson 2013). The CUC and its transport vary significantly over weeks and seasons to decades (e.g., Marchesiello et al. 2003; Collins et al. 2004; Meinvielle and Johnson 2013; Thomson and Krassovski 2015). Our purpose here is to assess the governors of the CUC transport and its variability from a momentum perspective.

Assessing the mechanisms of the CUC origin is useful for understanding and predicting the CUC transport variability. Several hypotheses about the coastal undercurrent origin have been proposed. Samelson (2017) discusses the role of the cross-shore pressure gradient in the development of a coastal undercurrent, during the quasigeostrophic adjustment to sea surface height (SSH) anomalies at the shelf break. Other studies have instead emphasized the important role of the alongshore pressure gradient, induced by remotely forced coastal-trapped waves and winds (e.g., Hickey and Pola 1983; Hill et al. 1998; Gay and Chereskin 2009; Connolly et al. 2014; Thomson and Krassovski 2015). Although the β effect in combination with a positive wind stress curl can lead to poleward flow through Sverdrup theory (e.g., Hurlburt and Thompson 1973; McCreary et al. 1987; Capet et al. 2004), in an idealized wind-driven stratified model with an eastern boundary, the alongshore pressure gradient and vertical mixing are instead the key elements to the origin of coastal undercurrents (McCreary 1981). Observations also indicate that the low-frequency fluctuations of the CUC can be attributed to the changes of the alongshore pressure gradient, induced by wind variability (Thomson and Krassovski 2015).

Modeling and observational studies show that the California Current region is highly turbulent with eddies (e.g., Garfield et al. 1999; Cornuelle et al. 2000; Barth et al. 2005; Capet et al. 2008; Colas et al. 2013; Collins et al. 2013; Molemaker et al. 2015; Renault et al. 2016a; Gómez-Valdivia et al. 2017; Chenillat et al. 2018). Moreover, these eddies show strong eddy–mean flow interactions (Renault et al. 2016c). Thus, we hypothesize that eddies play an indispensable role in modulating the CUC transport variability. We test this idea here by first examining the horizontal momentum balance to determine the influences from the eddy advection of momentum. Then, we assess whether topographic form stress is linked with the CUC transport and its variability, since theoretically, eddies can drive coastal undercurrents through topographic form stress (the so-called Neptune effect). In this scenario, the eddy–topography interaction leads to a topographic form stress that drives the large-scale mean flow (e.g., Holloway 1987, 1996; Salmon 1998; Maltrud and Holloway 2008; Wang and Stewart 2018).

Besides the roles of eddy advection and the Neptune effect, this study also examines the role of eddy stress in redistributing momentum throughout the CUC. An earlier study had argued that eddy stress, with a magnitude comparable to that of the wind stress, can transfer momentum vertically in the energetic ocean regions (e.g., western boundary currents), eventually being balanced by the topographic form stress (Ferreira et al. 2005). Other studies show that the eddy stress has an important role in the momentum balance of the Southern Ocean circulation (e.g., Danabasoglu et al. 1994; Stewart and

Corresponding author: Ru Chen, ruchen@alum.mit.edu

DOI: 10.1175/JPO-D-20-0234.1

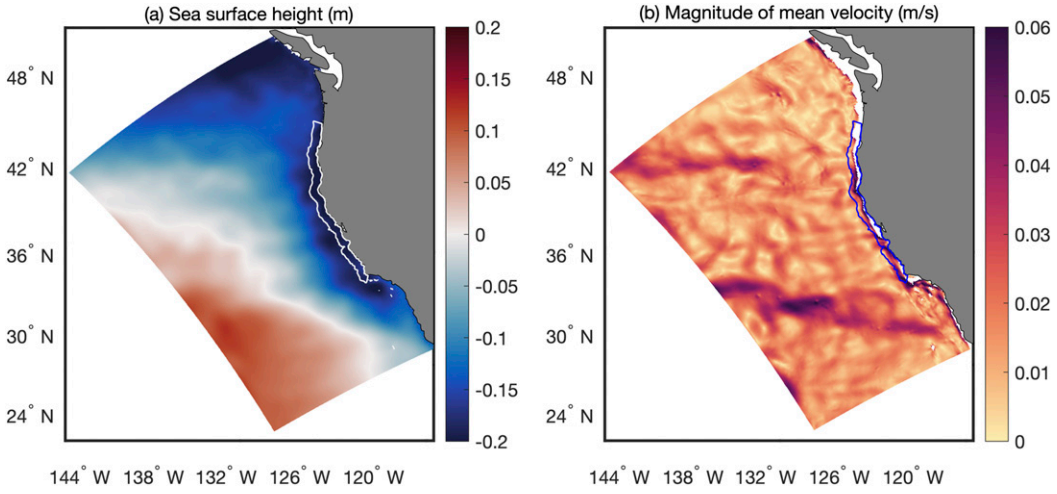

FIG. 1. The time-mean sea surface height (SSH) and the magnitude of the time-mean flow at 200 m from the USW4 solution. Here the time mean denotes the 16-yr temporal average over 1995–2010. The (a) white and (b) blue closed lines near the coast indicate the domain for this California Undercurrent (CUC) study, with an offshore distance of 0–60 km and the latitudinal range of 34.4°–44°N.

Thompson 2016; Wang and Stewart 2018). Consequently, here we suggest that eddy stress is probably important for redistributing momentum in the CUC region.

Duran (2019) investigates the dynamical balance of the CUC at 41°–48°N using the Regional Oceanic Modeling System (ROMS) (Shchepetkin and McWilliams 2005), showing that arrested topographic waves are needed to generate the poleward undercurrent. Here, we choose to analyze a mesoscale-resolving numerical solution using ROMS, which agrees well with observations (Renault et al. 2021). A realistic regional simulation has the advantages of 1) it includes many factors absent in idealized models (e.g., McCreary 1981; Connolly et al. 2014), 2) it has a higher spatiotemporal resolution than global models, and 3) the solution covers a larger area than hydrographic observations (e.g., the California Cooperative Oceanic Fisheries Investigations; Bograd et al. 2003), revealing a more complete picture.

This paper is organized as follows. Section 2 introduces the model configuration, and section 3 briefly depicts the CUC characteristics in the model. Sections 4 and 5 present the conventional momentum balance, including both the regional integral and vertical cross sections. In particular, the role of eddy advection in modulating the CUC transport variability is evaluated. Sections 6 and 7 present the roles of both the Neptune effect and the eddy stress. Section 8 is a summary.

2. Model configuration

The ROMS code algorithm is described in Shchepetkin and McWilliams (2005). No explicit horizontal mixing of momentum and tracer is specified, and the vertical mixing is parameterized using the K-profile parameterization (KPP) scheme (Large et al. 1994). The bathymetry dataset is based on the Shuttle Radar Topography Mission (SRTM30 plus) dataset (Becker et al. 2009). As topographic smoothing can improve the realism of simulated eddying flows (Penduff et al. 2002), we closely follow the approach in Renault et al. (2016c), smoothing the topographic data over a horizontal scale of 16 km to avoid aliasing.

Details of the model setup are available in Renault et al. (2021). In brief, we ran the simulation using a nesting approach, starting from a simulation at a resolution of 12 km. This starting simulation, called USW12, covers a domain larger than that in Fig. 1, and has initial and boundary conditions derived from the 0.25°, daily averaged global reanalysis product, Mercator Glorys2V3 (http://www.myocean.eu). Figure 1 shows the domain for the nested experiment USW4, which instead has a horizontal resolution of 4 km. This nested solution has 60 terrain- and surface-following sigma levels in the vertical with stretching parameters hcline = 250 m, $\theta_b = 3.0$, and $\theta_s = 6$ (Shchepetkin and McWilliams 2009). The initial and horizontal boundary conditions for the USW4 simulation is obtained from the coarser-resolution experiment USW12. We analyze the USW4 solution in its equilibrated state over the years 1995–2010, with vertical viscosity output absent in 2007–10. Therefore, the figures with vertical viscosity information (Figs. 6 and 8) are based on the model output during 1995–2006. However, the results, excluding viscosity, are insensitive to the choice of record length (12 vs 16 years).

The USW4 solution agrees well with satellite and in situ observations in the aspects of hydrography, mesoscale eddy activity, as well as the structures of both coastal upwelling and mean circulation (Renault et al. 2021). Compared with previous efforts simulating the California Current system using ROMS (e.g., Marchesiello et al. 2003; Capet et al. 2008; Colas et al. 2013), the USW4 solution here has two main advantages. One, the model is forced by realistic interannually varying, hourly atmospheric output that has a horizontal spatial resolution of 6 km from the Weather Research and Forecast (WRF) Model (Skamarock et al. 2008; Renault et al. 2016b, 2021). Two, to represent the current feedback to the atmosphere, the

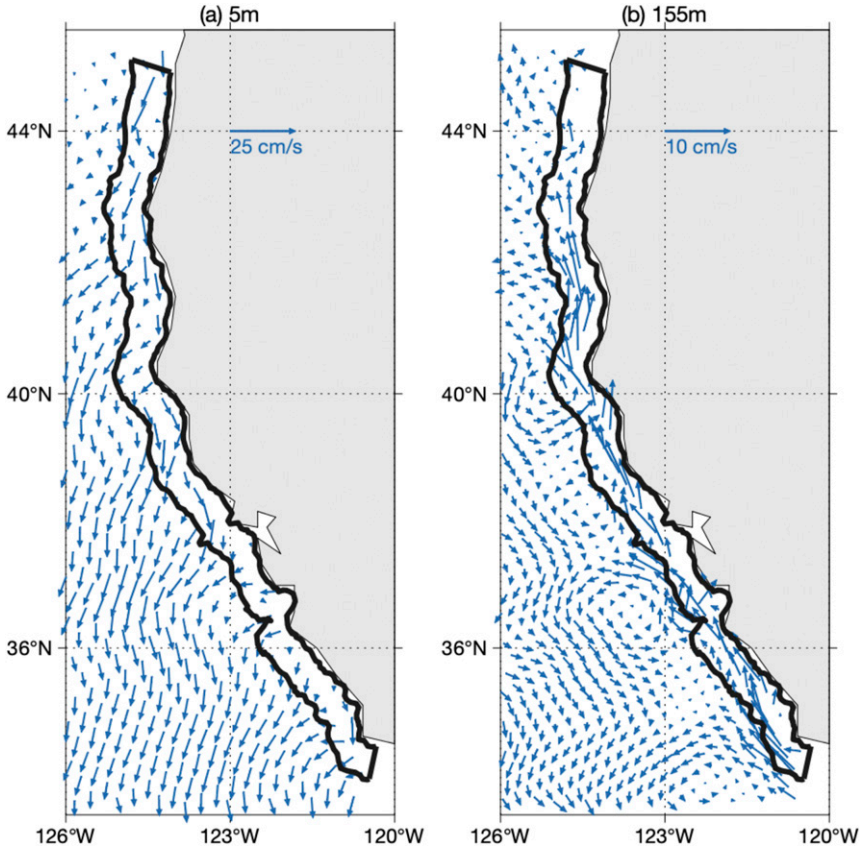

FIG. 2. The 16-yr (1995–2010) mean velocity vectors (blue arrows) from the USW4 solution. (a) At 5-m depth. (b) At 155-m depth. The black line bounds the selected CUC region for this study, as in Fig. 1.

simulation uses a parameterization based on a wind-correction approach (Renault et al. 2016c, 2020, 2021) that can induce realistic eddy damping. The simulation also includes the effect of wind drop off (Renault et al. 2016b).

3. Characteristics of the California Undercurrent

Figure 1 shows the time-mean SSH and magnitude of the time-mean velocity at 200 m from the USW4 solution. The closed contour near the California coast is the CUC region we focus on in this study: 0–60 km offshore at 34.4°–44.9°N. This region belongs to the eastern part of the subtropical gyre (Fig. 1a), with the near-surface, southward-flowing broad current being the California Current. Deeper (e.g., 155 m), the flow is poleward at the continental slope, with magnitude large right at the coast and decaying rapidly off coast (Figs. 1 and 2). Besides the CUC near the coast, the two zonal bands of mean flow in the domain interior are also intense (Fig. 1b).

An along-coast survey within a single year reported several characteristics of the CUC including a mean flow speed of $\sim$0.1 m s^{-1}, a core depth at about 200–275 m, a cross-shore scale of order of the first baroclinic Rossby radius of deformation [O(20) km], and a transport of 0.8 $\pm$ 0.2 Sv (1 Sv $\equiv 10^6$ m^3 s^{-1}) (Pierce et al. 2000). Other studies report similar values: a width of 30–50 km, strongest flow at 100–300 m, and transport on the order of one Sv (e.g., Reid 1962; Wooster 1970; Hickey 1979; Tsuchiya 1980; Chelton 1984; Lynn and Simpson 1987; Collins et al. 1996; Bray et al. 1999; Gay and Chereskin 2009). The CUC characteristics (e.g., width, speed, transport, and depth range) from the USW4 solution agree well with those previously reported values (not shown). As to the CUC's density, the simulation gives a range of 1025–1027 kg m^{-3}, roughly consistent with the 1026.4–1026.5 kg m^{-3} for the CUC core found by Gay and Chereskin (2009). The CUC structure from the USW4 solution is also consistent with observations and previous results (Renault et al. 2021), indicating that this solution is a reasonable tool to evaluate the dynamical balances of the CUC.

Due to the potential vorticity constraint, the CUC core approximately aligns with the 200-m isobath (e.g., R. Chen et al. 2021, unpublished manuscript). Hence, our analysis is mostly projected onto the direction aligning with (perpendicular to) the 200-m isobath, i.e., the along-isobath (cross-isobath) direction. The cross-section plots (e.g., Fig. 3) thus present variables as a function of depth and off-isobath distance, meaning the distance off the 200-m isobath. To be consistent, "offshore distance" hereafter refers to the cross-isobath distance to the

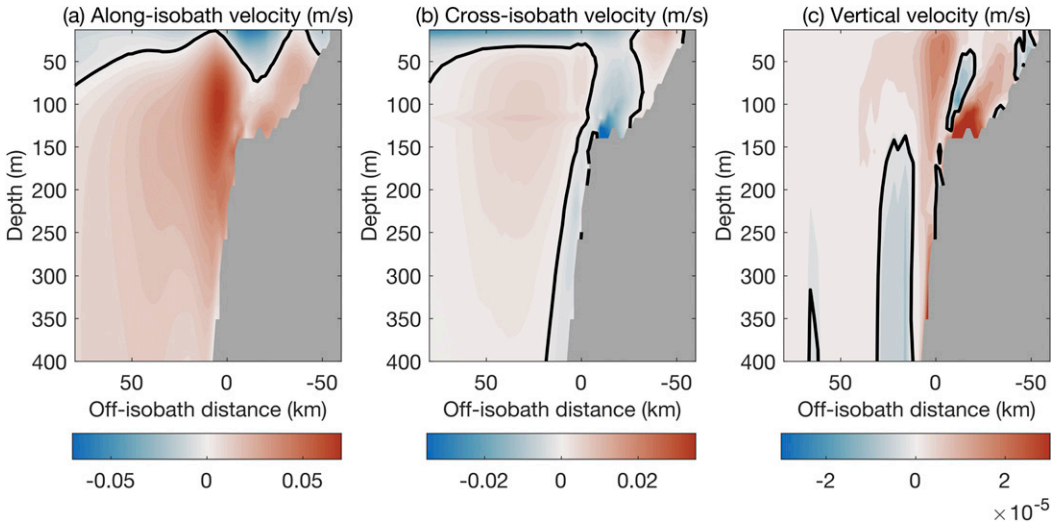

FIG. 3. The 16-yr (1995–2010) mean depth profiles of (a) along-isobath velocity, (b) cross-isobath velocity, and (c) vertical velocity ($m\,s^{-1}$). All are averaged along the 200-m isobath direction over the selected region (34.4°–44.9°N). The abscissa represents the distance off the 200-m isobath. Velocities presented here are those averaged over the grid points with the same off-isobath distance and depth in the selected region. The thick black contour indicates the zero value.

coastline. The CUC region (0–60 km offshore), enclosed by the black contours in Fig. 2, denotes the area with offshore distances ranging from 0 to 60 km.

Figure 3a shows the cross section of the time-mean along-isobath velocity averaged in the selected CUC region. Its magnitude within the CUC is on the order of $0.1\,m\,s^{-1}$. The CUC roughly locates at 50–400 m and near the 200-m isobath i.e., the location with zero off-isobath distance. Consistent with previous studies (e.g., Hickey 1979; Hickey and Pola 1983; Chelton 1984; Lynn and Simpson 1987; Gay and Chereskin 2009), the CUC here undergoes a significant seasonal cycle (Fig. 4), being much stronger in the summer and fall than that in the winter and spring. Also, the CUC depth is shallower in the winter than that in the summer. The spring CUC is narrow and mainly resides near the seafloor, whereas at the same depth, upon moving further offshore from the CUC, the flow reverses, pointing equatorward. This flow-reversal phenomenon in the spring mainly occurs north of 38°N. Details about the latitudinal variability of the CUC features are in R. Chen et al. (2021, unpublished manuscript).

The time-mean cross-isobath flow, much weaker than the along-isobath flow, has a different structure (Fig. 3b). It is mostly offshore in the upper 50 m due to the Ekman flow driven by the equatorward wind stress. Though the cross-isobath flow is mostly inshore below 50 m away from the bottom topography, there is offshore flow occurring right at the seafloor near the 150-m isobath, leading to the convergence of cross-isobath flow. This flow convergence phenomenon occurs sporadically, but is prevalent in the latitude range in the selected CUC region and consistent with the strong vertical velocity here. The transverse (cross-shore and vertical) circulation of a coastal undercurrent is typically characterized by upwelling-offshore flow near the surface and downwelling-inshore flow near the bottom boundary layer (e.g., McCreary 1981; Werner and Hickey 1983). Though these features also exist here, the CUC also shows a band of near-bottom flow in the offshore and upward direction at approximately 150–400 m (Fig. 3). The occurrence of this band suggests some near-bottom convergence of the along-isobath flow there.

We define the CUC transport as the integral of the along-isobath velocity over depths of 50–500 m and within 60 km offshore, based on the CUC structure. In the cross sections of the along-isobath velocity as a function of off-isobath distance and depth, the CUC becomes clear only when the flow is averaged over periods of 3 months or more. Therefore, we use a 3-month average for the transport estimate. For the results in Fig. 5, we also average over the entire selected CUC region. Thus, eddy influences have been effectively removed from these CUC transport results. The time-mean CUC transport (red line) is 0.4 Sv, and the maximum value reaches 1.5 Sv. The snapshot-like observations of Pierce et al. (2000) fall within the range of the transport values identified here. The CUC transport varies significantly over seasonal to interannual time scales, with a spectrum peak at the seasonal cycle (red line in Fig. 5a). However, seasonal variability is not the dominant component here as it accounts for only 9.0% (12.5%) of the transport variability when integrated over the entire water column (50–500 m).

4. Momentum balance diagnostic framework

The momentum equation, consistent with the ROMS model setup and projected onto $\hat{\mathbf{a}}$, the direction aligning with the 200 m isobath, is

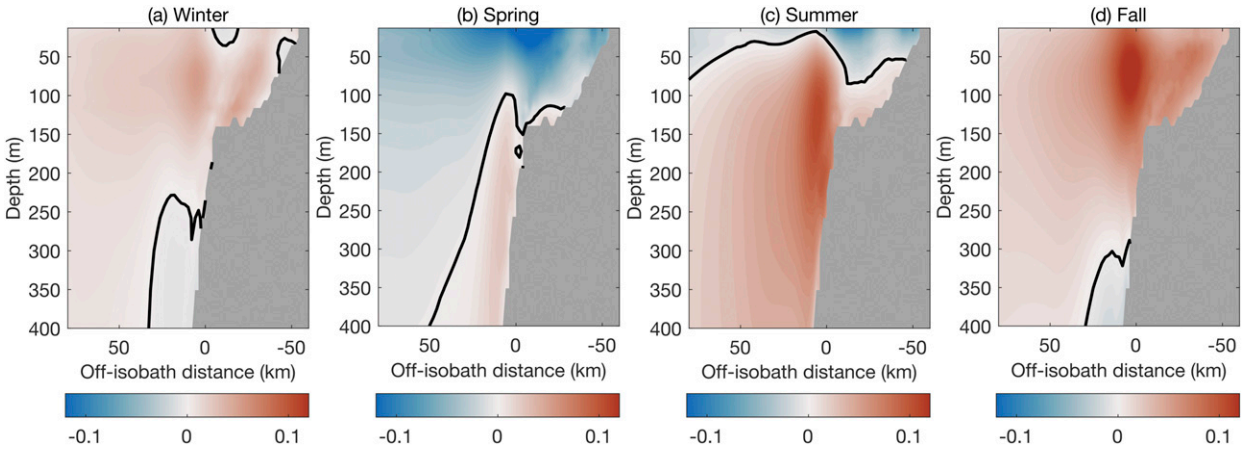

FIG. 4. As in Fig. 3a, but for the along-isobath velocity (m s^{-1}) temporally averaged over each season during 1995–2010. The horizontal axis indicates the distance off the 200-m isobath. Here, winter, spring, summer, and fall denote January–March, April–June, July–September, and October–December, respectively. Thick black contours represent the zero value.

$$\underbrace{\partial_t \mathbf{u}\cdot\hat{\mathbf{a}}}_{\text{tendency}} = \underbrace{-(\mathbf{u}_3\cdot\nabla_3\mathbf{u})\cdot\hat{\mathbf{a}}}_{\text{advection}} \underbrace{-(f\hat{\mathbf{z}}\times\mathbf{u})\cdot\hat{\mathbf{a}}}_{\text{Coriolis}} \underbrace{-(\nabla p/\rho_0)\cdot\hat{\mathbf{a}}}_{\text{pressure}} + \underbrace{\partial_z(A_v\partial_z\mathbf{u})\cdot\hat{\mathbf{a}}}_{\text{mixing}}, \quad (1)$$

where $\hat{\mathbf{a}}$ represents the along-isobath direction, $\hat{\mathbf{z}}$ is a unit vector in the vertical direction, $\mathbf{u}_3$ the three-dimensional velocity, ∇_3 the three-dimensional differential operator, $\mathbf{u}$ horizontal velocity, f the Coriolis parameter, ρ_0 the reference density in the model ($1027.4\,\text{kg}\,\text{m}^{-3}$), p total pressure, and A_v is the spatiotemporally varying vertical viscosity. Horizontal mixing is ignored in Eq. (1), because the explicit horizontal viscosity is set to be zero in this experiment. Due to the potential vorticity constraint, the CUC mostly flows along topography, with its core aligning with the 200-m isobath (R. Chen et al. 2021, unpublished manuscript). Therefore, we evaluate the "along-isobath" instead of the "along-shore" momentum equation. However, the key conclusions are insensitive to this choice.

The spatiotemporal average of Eq. (1) is simply

$$\frac{\int_{\hat{\mathbf{V}}}\partial_t\overline{\mathbf{u}}\cdot\hat{\mathbf{a}}\,dV}{|\hat{\mathbf{V}}|} = \frac{\int_{\hat{\mathbf{V}}} -\overline{(\mathbf{u}_3\cdot\nabla_3\mathbf{u})}\cdot\hat{\mathbf{a}} - (f\hat{\mathbf{z}}\times\overline{\mathbf{u}})\cdot\hat{\mathbf{a}} - \nabla\overline{p}/\rho_0\cdot\hat{\mathbf{a}} + \partial_z(\overline{A_v\partial_z\mathbf{u}})\cdot\hat{\mathbf{a}}\,dV}{|\hat{\mathbf{V}}|}, \quad (2)$$

where $\int_{\hat{\mathbf{V}}}\cdot\,dV/|\hat{\mathbf{V}}|$ denotes the average over the volume $|\hat{\mathbf{V}}|$. In general, an overbar denotes a temporal average, a prime refers to deviation from the time mean, a vector with a "3" subscript includes both horizontal and vertical components, whereas bold font without the subscript 3 denotes a horizontal vector. Replacing $\hat{\mathbf{a}}$ from Eqs. (1) and (2) by the cross-isobath direction $\hat{\mathbf{c}}$ leads to the cross-isobath diagnostic framework. Due to the CUC direction, the along-isobath momentum budget is more relevant to the CUC dynamics than the cross-isobath counterpart. Nevertheless, for completeness we estimate the momentum budget in both directions.

We choose the specific spatiotemporal averaging for Eq. (2) to fit both the CUC characteristics and our research goal. For example, for the cross-section plots resolving the spatial structure of the momentum balance (Figs. 9, 10, and 13), we choose to average over either the entire 16-yr record or over all 16 years of each individual season. In these cases, the spatial average refers to the along-isobath average over the selected CUC region. However, to study the governors of the CUC transport variability, we diagnose the time series of each momentum balance term and then estimate its time mean, seasonal cycle, and its temporal correlation with the along-isobath velocity strength (Figs. 6–8, 11, and 12). As the CUC lies mainly within 60 km offshore (section 3), we choose the volume $|\hat{\mathbf{V}}|$ to be 0–60 km offshore over the entire water column in the selected CUC region (closed black contours in Fig. 2) for these time series. The CUC is clearly visible in the cross sections of along-isobath velocity only if we average the along-isobath velocity over periods of 3 months or more (section 3). Therefore, we choose the temporal averaging period to be 3 months. This is not a moving average, so each time series has four data points per year, each of which represents results in one season in a specific year. The seasonal cycle shown in Figs. 6, 7, and 11 is obtained by averaging data in the same season. Removing the seasonal cycle leads to the time series excluding the seasonal cycle (Figs. 8 and 12).

Consider the along-isobath transport. Figure 5 shows that this transport integrated over 50–500 m closely follows that integrated over the entire water column (correlation coefficient of 0.92–0.97 at the 95% confidence level). Therefore, for simplicity we integrate over the entire water column to obtain the time series used in Figs. 6–8, 11, and 12. In addition, we find

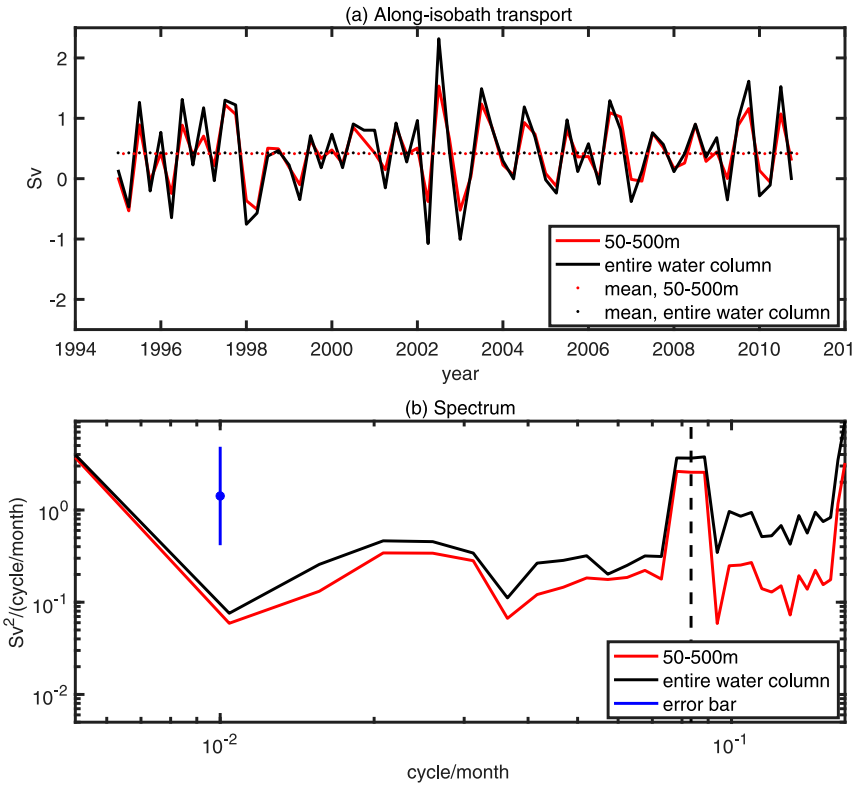

FIG. 5. (a) The along-isobath transport within 60 km offshore in the selected region integrated over 50–500 m (red) and over the entire water column (black) (34.4°–44.9°N) during the years 1995–2010, at a 3-month temporal interval. Horizontal dotted lines are the corresponding time-mean values. (b) The corresponding frequency spectrum of the time series from (a). The blue solid line with a dot denotes the error bar at the 95% confidence level, and the vertical black dashed line is the annual frequency.

that our conclusions hold, if averaging over 0–80 km or 0–100 km offshore. Equation (2) is essentially the governing equation for the volume-averaged velocity strength, not the CUC transport. However, the normalized CUC transport differs negligibly from the normalized volume-averaged velocity strength. ''Normalization'' here refers to dividing the time series by its maximum absolute value.

One can evaluate the role of eddies in modulating the CUC transport (section 5b) by decomposing the total advection $-(\mathbf{u}_3 \cdot \nabla_3 \mathbf{u})$ into a mean advection $-(\overline{\mathbf{u}}_3 \cdot \nabla_3 \overline{\mathbf{u}})$ and an eddy advection. This mean advection denotes the advection of the time-mean flow by the time mean flow. As such, the eddy advection is the deviation of total advection from the mean advection. Eddies are defined here as the deviation from the time mean (i.e., transient motions), including seasonal variability. This definition has been widely used due to its simplicity and analytical tractability (e.g., Wunsch 1998; Storch et al. 2012; Zhai and Marshall 2013; Halo et al. 2014; Chen et al. 2016). However, some studies define eddies as transient motions excluding the seasonal variability (Zhan et al. 2016). As the seasonal varying flow only accounts for 2.6% of total eddy kinetic energy at 50–500 m in the CUC region, we find that our key findings (e.g., the amplitude of eddy advection and its significant correlation with the CUC transport) are essentially the same with either eddy definition.

5. Momentum balance results

Here we present results regarding the conventional momentum budget [Eqs. (1) and (2)]. We find that eddy advection of momentum greatly modulates the temporal variability of CUC transport.

a. Regional integral

Figure 6 shows the along-isobath momentum balance volume averaged over the CUC region. The dominant balance is among the Coriolis force, pressure gradient and vertical mixing. The pressure gradient acts to accelerate the CUC, indicating that the along-isobath pressure gradient contributes to the CUC origin, as stated in McCreary (1981). The along-isobath pressure gradient is poleward in all the four seasons, with the largest magnitude in the summer due to the CUC strengthening. The Coriolis force and vertical mixing terms act to decelerate the CUC.

The vertical mixing term integrated over the entire water column is essentially the difference between the surface wind

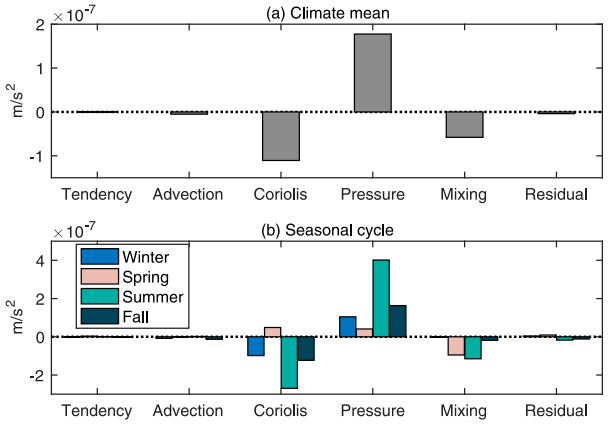

FIG. 6. (a) The 12-yr (1995–2006) mean for the along-isobath momentum balance terms volume averaged over the selected CUC region and the entire water column. (b) As in (a), but for the seasonal cycle. The terms on the abscissa are defined in Eq. (1). "Residual" here refers to the imbalanced part in the diagnosis due to numerical and diagnostic errors, and the use of daily averaged output.

stress and bottom drag divided by density. In contrast to the negligibly weak along-isobath bottom drag (not shown), the along-isobath wind stress at the CUC is large and points equatorward. Therefore, the vertical mixing term, integrated over the entire water column, points equatorward with noticeable magnitude (Fig. 6a). Yet, the along-isobath momentum budget integrated over 50–500 m is nearly geostrophic, with negligible vertical mixing (not shown).

The cross-isobath momentum budget integrated over the entire column or over 50–500 m (not shown) is nearly in geostrophic balance partially due to the small magnitude of the cross-isobath wind stress. We would expect this dominance of geostrophic balance due to the large spatial domain and long time average used in Eq. (2). Similar to the along-isobath case, the cross-isobath pressure gradient also has the largest magnitude in the summer.

b. *Advection: One governor of CUC variability*

The time and season mean of the advection and tendency terms are of the same order of magnitude, though both small (Fig. 6). Nevertheless, we argue that advection, particularly eddy advection, can be important in setting both the time mean and temporal variability of the CUC. Their important role arises because eddies in the turbulent ocean tend to modulate the ocean circulation through eddy–mean flow interaction.

Consider the net advection of the along-isobath velocity (v) and cross-isobath velocity (u). The total advection in Fig. 7 is dominated by eddy advection for both the along-isobath and cross-isobath momentum balances. The eddy advection of v acts in the opposite direction of the time-mean CUC, thus opposing the along-isobath pressure gradient (Figs. 6a and 7a). Both eddy and mean advection of u act to accelerate the inshore flow and decelerate the offshore flow. Advection varies seasonally, with eddy advection of v peaking in fall and eddy advection of u peaking in summer.

We now evaluate the potential role of each momentum term in modulating the CUC variability. In Fig. 8 we diagnose the ordinary correlation between the tendency term time series, indicating the CUC variability, and other momentum terms

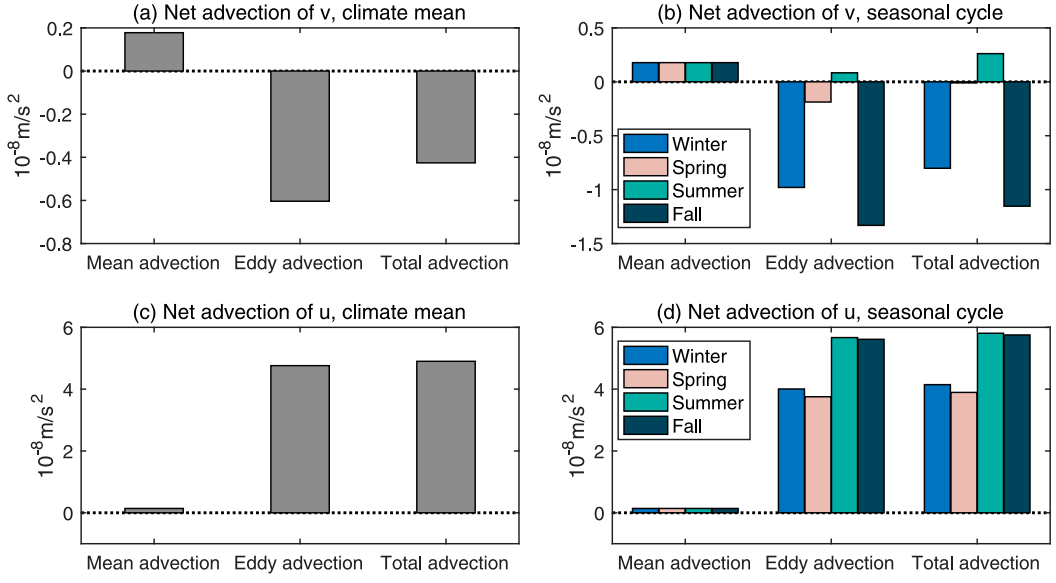

FIG. 7. The (left) 16-yr mean and (right) seasonal mean of the advection term in the momentum balance equations for the (upper) along-isobath velocity v and (lower) cross-isobath velocity u. Results here are those volume averaged over the selected CUC region and the entire water column. Total advection, defined in Eq. (1), is decomposed into mean advection and eddy advection (section 4). Positive advection of v indicates advection acts to accelerate the CUC. Positive advection of u indicates advection acts to accelerate the inshore flow.

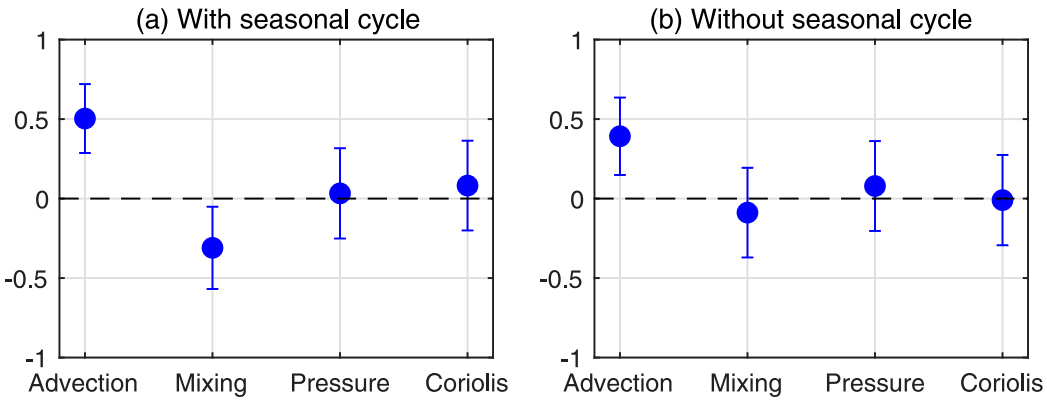

FIG. 8. Correlation coefficients between the temporal change rate of the along-isobath velocity strength (tendency term) and the other along-isobath momentum terms marked on the abscissa and defined in Eq. (1). (a) Includes the seasonal cycle. (b) As in (a), but the seasonal cycle of the time series was removed before estimating the correlation coefficients. The time series of the momentum terms used here is those integrated over the entire depth range of the selected CUC region during 1995–2006. The error bars indicate uncertainties at the 95% confidence level.

(e.g., advection). (The method to obtain the time series is described in section 4.) The net advection of the along-isobath velocity correlates positively with the CUC transport variability, having the largest correlation magnitude among the four terms (Fig. 8a). The correlation is still statistically significant when seasonal variability is excluded in the time series (Fig. 8b). The correlation between the Coriolis force and the CUC transport is insignificant. Though the along-isobath pressure gradient acts in the direction of the time-mean CUC, it is not significantly correlated with the CUC variability. However, the topographic form stress component of the along-isobath pressure gradient is significantly correlated with the CUC variability (section 6).

When seasonal variability is included, the vertical mixing term is statistically significantly correlated with the CUC transport (Fig. 8). As the along-isobath vertical mixing integrated over the entire water column is essentially the difference between the surface wind stress and bottom drag divided by density, with wind stress dominating, this result indicates that the seasonally varying along-isobath wind stress probably contributes to the seasonal variability of the CUC transport. This finding is consistent with studies finding an important role of the alongshore wind stress in the undercurrent formation (e.g., McCreary et al. 1987; Gay and Chereskin 2009). Though the wind stress curl can contribute to the CUC origin through the Sverdrup balance mechanism, a poleward undercurrent can be generated in a stratified system forced by the equatorward wind stress without curl (McCreary 1981; Chelton 1982; McCreary et al. 1987; Bray et al. 1999). The mechanism that the winds drive the seasonally varying CUC has longitudinal variability (Marchesiello et al. 2003). It is unclear, however, why significant correlation occurs only when seasonal variability is included (Fig. 8b).

c. *Cross-shore structure*

Figure 9 shows the cross section of the time-mean momentum terms. Consistent with the volume integrated results above, the along-isobath pressure gradient accelerates the time-mean CUC within the CUC core, in opposition to the decelerating influence from eddy advection. The difference between the pressure gradient and Coriolis terms is small except near the ocean surface and bottom. At these locations, the vertical mixing of momentum is elevated because of surface wind stress and bottom drag. Within the CUC, geostrophic balance generally holds. Though the net advection of the along-isobath velocity varies by season, advection always retards the CUC core (Fig. 10). Geostrophic balance generally holds for the cross-isobath momentum balance (Figs. 9e–h). In contrast with the along-isobath scenario, the cross-isobath pressure gradient retards the cross-isobath flow and advection accelerates it (Figs. 3 and 9).

In the region off the Washington–Oregon coast, the momentum balance varies with the offshore distance (Werner and Hickey 1983). The results in Fig. 9 agree, showing that the momentum balance differs between slope and shelf. We quantify this difference by dividing the CUC region (0–60 km offshore) into slope and shelf regions, separated by the 150 m isobath, and then repeating the momentum analysis for each region. The results for the slope region closely match the entire-volume case shown in Figs. 6–8 because the CUC core mostly resides on the slope (Fig. 3). Therefore, our choice of $|\hat{\mathbf{V}}|$ from section 4 is suitable for examining the CUC.

6. Role of topographic form stress

By diagnosing the topographic form stress, we show here that the Neptune effect helps to drive the CUC's time mean and temporal variability.

a. *The Neptune effect and topographic form stress*

Systematic topographic form stress can be generated through eddy–topography interaction and that then influences the large-scale circulation (e.g., Holloway 1987, 1996). This effect,

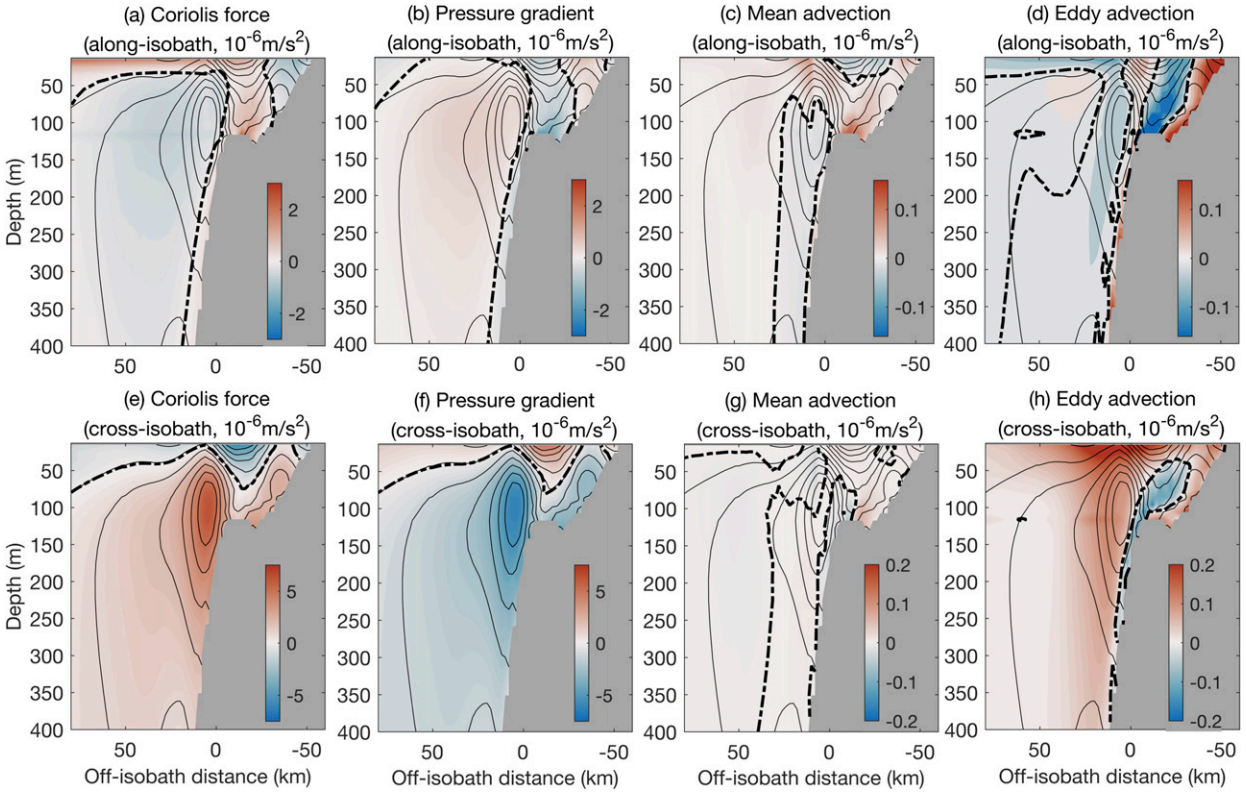

FIG. 9. Cross sections, as a function of off-isobath distance and depth, of the 16-yr mean (a) Coriolis force, (b) pressure gradient, (c) mean advection, and (d) eddy advection from the along-isobath momentum balance, along-isobath averaged over the selected CUC region. These terms are defined based on Eq. (1). "Mean advection" denotes the advection of mean flow by the mean flow, and "eddy advection" denotes the difference between total advection and mean advection. (e)–(h) As in (a)–(d), but for the cross-isobath momentum balance. The thick dashed black contour in each panel represents the zero value of the corresponding term. The thin solid black contours are those of the 16-yr mean along-isobath velocity, indicating the CUC location. The abscissa is the distance off the 200-m isobath.

called the Neptune effect, has been shown to significantly modify the mean flow in numerical models (e.g., Holloway 1992; Holloway and Wang 2009). Indeed, Holloway (1987) hypothesizes that the Neptune effect can be a dominant mechanism driving coastal undercurrents. Here, we test the validity of this hypothesis in the CUC through diagnosing topographic form stress (appendix A) using the USW4 solution.

The volume integrated along-isobath pressure gradient can be decomposed as

$$-\frac{1}{\rho_0}\int_{\hat{\mathbf{V}}}\partial_y p' dV = D_{\text{side},a} + D_{\text{topo},a} = \text{SSH}_a + \text{BC}_a, \qquad (3)$$

where p' is the deviation of total pressure from the spatially averaged pressure value at each depth over the entire region (appendix A). The term $D_{\text{topo},a}$ denotes the along-isobath topographic form stress and $D_{\text{side},a}$ is the along-isobath pressure force acting on the side of the volume $\hat{\mathbf{V}}$ [Eq. (A7)]. The terms SSH_a and BC_a respectively denote the along-isobath pressure gradient induced by SSH tilting and isopycnal tilting [Eq. (A10)]. Similarly, we decompose the cross-isobath pressure gradient into $D_{\text{side},c} + D_{\text{topo},c}$ or $\text{SSH}_c + \text{BC}_c$, where the subscript c is the same as subscript a except for the cross-isobath direction [Eqs. (A11) and (A12)].

b. Results

Figure 11 presents the time-mean decomposition of pressure gradients. Both the topographic form stress $D_{\text{topo},a}$ and the lateral-boundary pressure component $D_{\text{side},a}$ act in the direction of the time-mean CUC, with comparable magnitudes. They both reach the largest magnitude in the summer when the CUC is strengthening. In the cross-isobath direction, both $D_{\text{topo},c}$ and $D_{\text{side},c}$ are negative, pointing offshore. By dividing the entire selected CUC region into several subdomains, each of which covers a 2° latitude range, we obtain the latitudinal distribution of $D_{\text{topo},a}$. We find that $D_{\text{topo},a}$ is positive in all the subdomains, indicating that the Neptune effect is a prevalent contributor to the CUC in our study domain.

A positive $D_{\text{topo},a}$ means a positive correlation between the pressure anomaly and topography variation [Eq. (A7)]. Holloway (1987) provides a heuristic explanation of the Neptune effect from the perspective of vorticity–topography interaction, vorticity wave propagation, and topographic scattering, using the principle of potential vorticity conservation

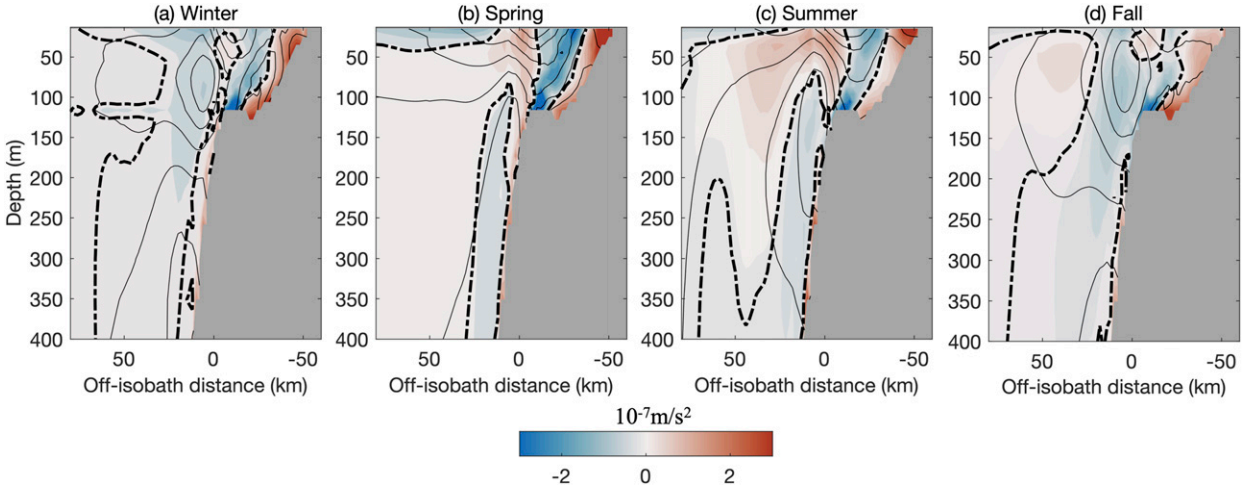

FIG. 10. Cross sections of total advection in each season in the along-isobath momentum balance over the selected CUC region. The spatiotemporal average is the same as that in Fig. 4. The thick dashed black contour in each panel represents the zero value of the corresponding term. The thin solid black contours are those of the along-isobath velocity in each season during 1995–2010, indicating the CUC location in each season. The abscissa is the distance off the 200-m isobath.

and the idea of momentum transfer through pressure–slope relation. Rigorous derivation about these processes is also provided by Holloway (1987, 1992) in the quasi-geostrophic framework. Including this Neptune effect in coarse-resolution models can lead to a stronger CUC (Maltrud and Holloway 2008).

The along-isobath topographic form stress ($D_{\text{topo},a}$) significantly correlates with the transport variability, regardless of whether seasonal variability is included (Fig. 12), indicating the relevance of the Neptune effect to the CUC variability. Though both $D_{\text{topo},a}$ and $D_{\text{side},a}$ act in the direction of the time-mean CUC, only $D_{\text{topo},a}$ greatly modulates the temporal variability of the CUC transport.

The pressure gradient can also be decomposed into SSH tilting and isopycnal tilting components [Eq. (3)]. Overall, both

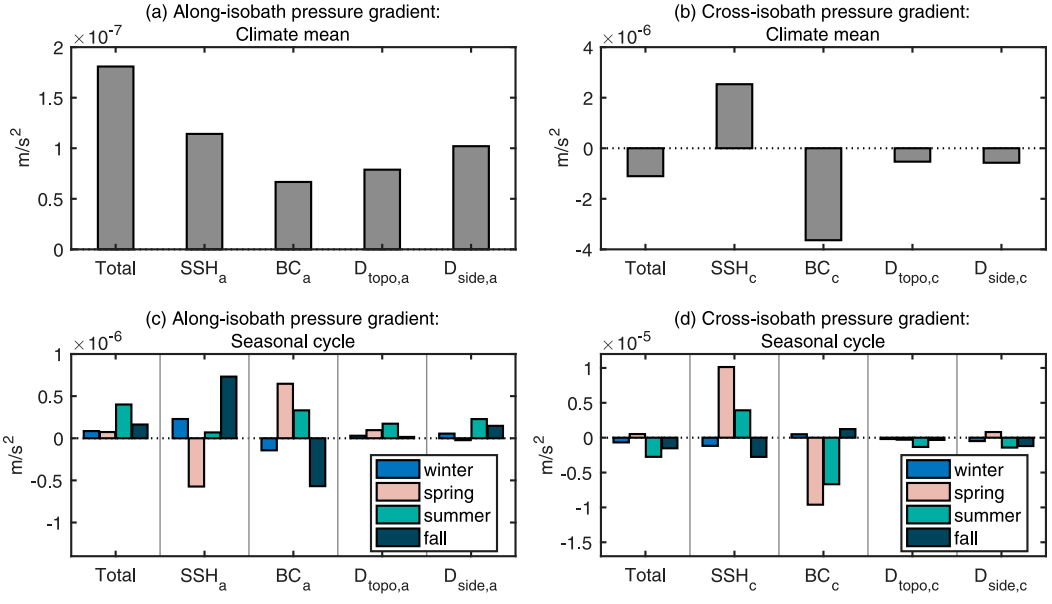

FIG. 11. The (top) 16-yr mean and (bottom) seasonal mean of the total pressure gradient decomposition volume averaged over the selected CUC region throughout the water column in the (a),(c) along- and (b),(d) cross-isobath directions. "Total" on the horizontal axis refers to the total along-isobath [in (a) and (c)] and cross-isobath [in (b) and (d)] pressure gradient. The pressure gradient terms on the abscissas are defined below Eq. (3) and in appendix A. To be consistent with Eq. (2) and the bar plots of the conventional momentum balance in section 5, D_{topo}, D_{side}, SSH, and BC are divided by $\hat{\mathbf{V}}$.

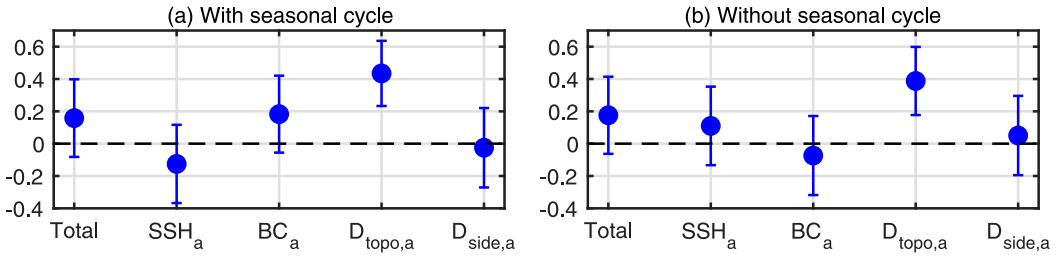

FIG. 12. Correlation coefficients between the along-isobath velocity strength change rate and, on the abscissa, components of the along-isobath pressure gradient. The components are defined below Eq. (3) and in appendix A. The time series used for the correlation diagnosis span the years 1995–2010 and are those integrated over the entire water column in the selected CUC region. The error bars indicate uncertainties at the 95% confidence level. (a) Includes the seasonal cycle. (b) As in (a), but with the seasonal cycle removed from the time series.

SSH_a and BC_a act to accelerate the CUC, but not during every season (Fig. 11). In particular, SSH_a retards the CUC in the spring, but accelerates it in the fall. The BC_a term does the opposite. The seasonal cycle of the total along-isobath pressure gradient is a net effect of this compensation. The compensation also occurs in the cross-isobath direction: 1) the time-mean SSH_c points inshore, whereas BC_c points offshore, and 2) both SSH_c and BC_c have the largest magnitude in the spring and summer, though pointing toward different directions (Fig. 11). Finally, neither SSH_a nor BC_a correlate with the CUC transport variability (Fig. 12).

7. Eddy stress

a. Diagnostic method

As a recap, the surface wind stress is equatorward, retarding the CUC, whereas the along-isobath pressure gradient including the topographic form stress is poleward, accelerating the CUC. For the Antarctic Circumpolar Current (ACC), however, the momentum input is the surface wind stress and the momentum sink is the topographic form stress. In this case, eddy stress helps to transfer downward the momentum gained from the wind (e.g., McWilliams et al. 1978; Tréguier and McWilliams 1990; Wolff et al. 1991; Ferreira et al. 2005). After comparing the CUC with the ACC scenario, we suggest that eddy stress probably also plays a role in redistributing momentum within the CUC. Motivated by this idea, we now evaluate the eddy stress in the CUC region.

Appendix B shows that, if we relax the zonal periodicity assumption that is often used in ACC studies, but keep the adiabatic, quasigeostrophic flow assumptions (e.g., small isopycnal slope), the mean eddy stress can be diagnosed from

$$\overline{\boldsymbol{\tau}}_e = -f\hat{\mathbf{z}}\times\frac{\overline{\mathbf{u}'b'}}{\partial_z\overline{b}}. \tag{4}$$

Our reformulated momentum and buoyancy balances, appropriate to the CUC region [Eqs. (B6) and (B7)], differ from the residual-mean model in Ferreira et al. (2005). However, the eddy stress formulation used in this study [Eq. (4)] is consistent with Ferreira et al. (2005). The eddy force $\mathbf{J}$, which is part of the reformulated momentum balance [Eq. (B6)], is simply

$$\mathbf{J} = \partial_z\overline{\boldsymbol{\tau}}_e. \tag{5}$$

By fitting dynamics to observations, Ferreira et al. (2005) estimated the global distribution of eddy stress, finding that in energetic regions (e.g., ACC, western boundary currents), eddy stress can transfer momentum from near the ocean surface downward with a magnitude comparable to the wind stress. In fact, in the zonally averaged case (e.g., reentrant channel), the eddy stress $\overline{\boldsymbol{\tau}}_e$ is often interpreted as the isopycnal form stress (i.e., the horizontal pressure force exerted onto the fluctuating isopycnal surfaces), which transfers momentum vertically (e.g., Vallis 2016; Stewart and Thompson 2016). Inspired by these previous studies, we consider the link between eddy stress and isopycnal form stress in regions with no zonal periodicity (e.g., CUC) (appendix C).

Our derivation shows that in the horizontally nonuniform regions, eddy stress cannot only redistribute momentum vertically, as the conventional isopycnal form stress defined in Ward and Hogg (2011), but also redistribute momentum horizontally (appendix C). Specifically, the eddy stress $\overline{\boldsymbol{\tau}}_e$ can be divided into an isopycnal form stress term $\overline{\boldsymbol{\tau}}_d$ and the term $\overline{\boldsymbol{\tau}}_{\mathrm{div}}$,

$$\overline{\boldsymbol{\tau}}_e \approx \underbrace{\frac{1}{\rho_0}\overline{p'\nabla\eta'}}_{\overline{\boldsymbol{\tau}}_d} \underbrace{-\frac{1}{\rho_0}\nabla\overline{(p'\eta')}}_{\overline{\boldsymbol{\tau}}_{\mathrm{div}}}, \tag{6}$$

where η' is the vertical fluctuation of a certain isopycnal and p' is the pressure anomaly. The term $\overline{\boldsymbol{\tau}}_{\mathrm{div}}$ is the spatial gradient of the correlation between pressure and the vertical displacement of the isopycnal surface. As discussed in appendix C, a similar decomposition of eddy-induced velocity in isopycnal coordinates appears in Greatbatch (1998).

b. Eddy stress in the CUC

In the CUC region, both the magnitude and spatial structure of eddy-induced velocities, which are linked with eddy stress [Eqs. (B11) and (B12)], are generally consistent with those in Colas et al. (2013). Thus, here we focus on eddy stress instead. Given that the quasigeostrophic assumption is invalid near the ocean surface and bottom, volume integrated results, such as those in section 5, are inappropriate here. Instead, we present the vertical structure of eddy stress in the interior.

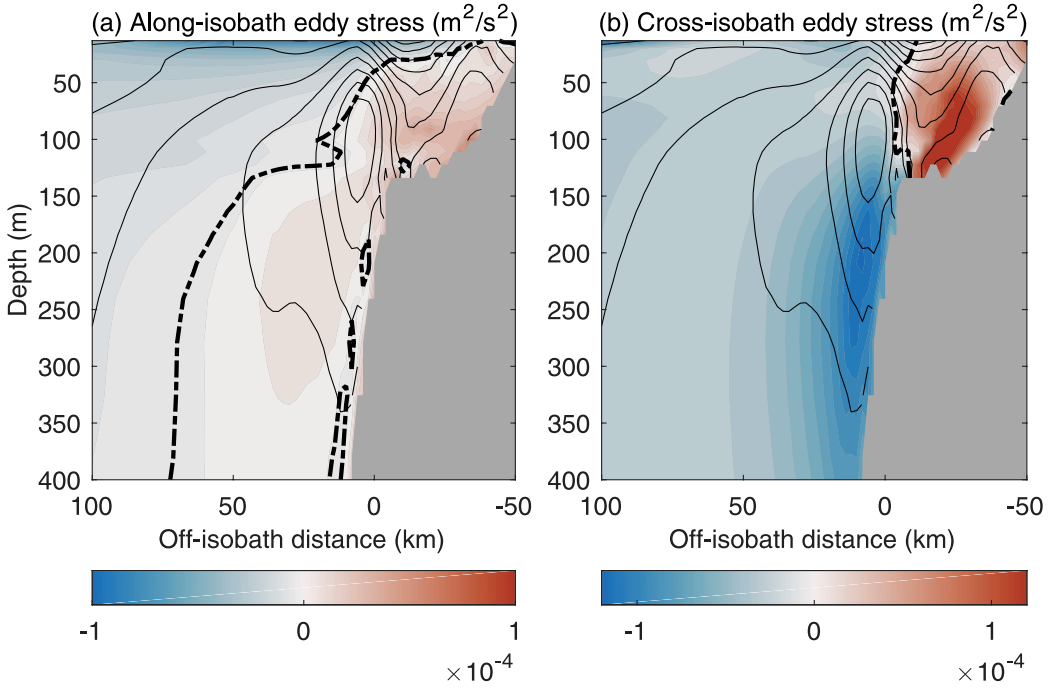

FIG. 13. The 16-yr mean (a) along-isobath and (b) cross-isobath eddy stress in the selected CUC region. The results here are obtained by projecting the mean eddy stress vector [Eq. (4)] onto the along-isobath and cross-isobath directions, and then along-isobath averaging them over the selected CUC region. The solid black contours denote the time-mean along-isobath velocity indicating the CUC location, and the dashed black contours mark zero eddy stress. The abscissa is the distance off the 200-m isobath.

Characteristics of the along-isobath eddy stress in the CUC region (Fig. 13a) suggests the vertical redistribution of momentum through eddy stress, which is analogous to the scenario proposed by Tréguier and McWilliams (1990) and Ferreira et al. (2005). In the along-isobath direction, eddy stress in the upper ocean gradually weakens with depth, and its equatorward direction is consistent with the wind stress direction. Also, the magnitude of the volume-averaged, along-isobath eddy stress in the upper 15 m ($5.0 \times 10^{-5}\,\mathrm{m^2\,s^{-2}}$) is close to that of the spatially averaged along-isobath wind stress divided by density ($4.1 \times 10^{-5}\,\mathrm{m^2\,s^{-2}}$). The similarity between eddy stress and wind stress indicates that the near-surface eddy stress acts to carry the equatorward momentum, extracted from the surface wind stress, down in the water column. Below the surface, eddy stress turns poleward within the CUC core and near the bottom. This turning indicates that eddy stress acts to transfer downward the poleward CUC momentum gained from the along-isobath pressure gradient. In the cross-isobath direction, eddy stress points inshore in the shallow region nearshore, and it points offshore in the relatively deep area offshore (Fig. 13b).

In addition, the eddy stress in the CUC region also acts to induce the horizontal transport of momentum in and out of the domain. This transport can occur because the term $\overline{\tau}_{\mathrm{div}}$ can redistribute momentum both horizontally and vertically [Eqs. (6) and (C4)]. Thus, to use a similar rationale as Greatbatch (1998), $\overline{\tau}_{\mathrm{div}}$ can be neglected compared to $\overline{\tau}_d$ when the horizontal scale of the oceanic current is much larger than the scale of eddies. Since the cross-shore scale of the CUC is comparable to the eddy scale (section 3), $\overline{\tau}_{\mathrm{div}}$ in the CUC region probably has magnitude comparable to $\overline{\tau}_d$. Thus, the $\overline{\tau}_{\mathrm{div}}$ term cannot be neglected and the horizontal redistribution of momentum through eddy stress cannot be ignored here.

Our diagnosis of eddy stress confirms the importance of $\overline{\tau}_{\mathrm{div}}$: In the CUC region, on the time-mean isopycnal surfaces ranging from 1025.6 to 1027.0 $\mathrm{kg\,m^{-3}}$ (typical density values within the CUC depth range), the ratio between the domain averaged $\overline{\tau}_{\mathrm{div}}$ and the domain averaged $\overline{\tau}_d$ in the along-isobath direction ranges from about 1.3 to 0.4, generally being larger when the density is lower. One caveat of this estimate is that part of the high-frequency pressure signal is missing due to the use of the monthly averaged SSH output when estimating pressure (daily SSH output is unavailable). In addition, as the isopycnal surface is a key variable in Eq. (6), the ratio between $\overline{\tau}_{\mathrm{div}}$ and $\overline{\tau}_d$ can be more accurately estimated using an isopycnal model than a model such as USW4 with terrain- and surface-following sigma levels. Despite these caveats, we conclude that to first-order, $\overline{\tau}_{\mathrm{div}}$ should not be neglected in the CUC region.

8. Summary and discussion

We evaluated the governors of the CUC transport from a momentum perspective, using an eddying regional model. Differing from the ACC, which is driven by the along-current wind stress and retarded by topographic form stress, the time-mean CUC is driven by both the topographic form stress and lateral-boundary pressure gradient while being retarded by the

along-isobath wind stress. Two important momentum governors of the CUC transport variability, ranging from intraseasonal to interannual time scales, are eddy momentum advection and topographic form stress, indicating that the Neptune effect applies to the CUC.

The eddy stress in the CUC region helps to transfer both the equatorward wind stress and the poleward CUC momentum downward. In addition, this study has a new theoretical finding: Eddy stress not only includes the isopycnal form stress, but also contains a spatial gradient term of the correlation between the pressure anomaly and isopycnal fluctuations, which can redistribute momentum horizontally (appendix C). Both the eddy stress theory and numerical diagnosis suggest that the horizontal redistribution of momentum through eddy stress cannot be neglected in the CUC region. Application of the eddy stress theory would help reveal the horizontal spread of momentum through eddy stress in energetic inhomogeneous regions (e.g., western boundary currents and topographic regions).

The key role of eddies identified here suggests that an accurate CUC prediction would require a realistic representation of the energy cascade and oceanic turbulence. Although the USW4 solution is not submesoscale resolving, we expect that the key conclusions presented here would remain hold in a submesoscale-resolving model. Nevertheless, it would be useful to assess the role of submesoscale processes in shaping the CUC transport. For example, internal wave generation and hydraulic flows can influence the dynamical balance in topographic regions (e.g., Naveira Garabato et al. 2013; Klymak 2018). Whether these processes can significantly influence the CUC is unclear.

This study can also be extended in two other directions. One, as the alongshore variability of wind, topography, and alongshore pressure gradient have been identified in this area (e.g., Checkley and Barth 2009; Connolly et al. 2014), the possible latitudinal variability of the CUC transport governors can be examined. Two, the California Current system can also be affected by the climate variability patterns and local wind stress (e.g., McCreary et al. 1987; Todd et al. 2011). For example, ENSO can influence this region through atmospheric teleconnection and coastal-trapped waves (Frischknecht et al. 2015). Therefore, a study should examine how climate indices or local wind stress can influence the CUC transport variability by changing the hydrographic states and consequently the momentum balance.

Acknowledgments. We acknowledge the support from the National Science Foundation (OCE1419450) and the National Natural Science Foundation of China (42076007).

Data availability statement. The USW4 solution, analyzed in this study, is available upon request from the corresponding author (R. Chen). It is not posted on a public website due to its large size.

APPENDIX A

Decomposition of Pressure Gradient Force

We start from the vector form of the momentum equation in the ROMS model,

$$\partial_t \mathbf{u} + \mathbf{u}_3 \cdot \nabla_3 \mathbf{u} + f\hat{\mathbf{z}} \times \mathbf{u} = -\frac{1}{\rho_0}\nabla_3 p - \hat{\mathbf{z}}\frac{g\rho}{\rho_0} + \partial_z(A_v \partial_z \mathbf{u}), \quad \text{(A1)}$$

where $\mathbf{u}$ is horizontal velocity, $\mathbf{u}_3$ is the three-dimensional velocity, p total pressure, ρ total density, A_v vertical viscosity, and ρ_0 is the reference density in the ROMS model ($1027.4\,\mathrm{kg\,m^{-3}}$), and

$$p(\mathbf{x}, z, t) = \hat{p}(z, t) + p'(\mathbf{x}, z, t), \quad \text{(A2)}$$

where $\hat{p}(z, t)$ is the spatial average of total pressure p over the entire selected CUC region at a constant depth at each time step and p' is the deviation of p from $\hat{p}$. In consequence,

$$\rho(\mathbf{x}, z, t) = \hat{\boldsymbol{\rho}}(z, t) + \rho'(\mathbf{x}, z, t) = -\frac{1}{\rho_0 g}\frac{\partial}{\partial z}\hat{p}(z, t) + \rho'(\mathbf{x}, z, t). \quad \text{(A3)}$$

The momentum equation [(A1)] can then be transformed into

$$\partial_t \mathbf{u} + \mathbf{u}_3 \cdot \nabla_3 \mathbf{u} + f\hat{\mathbf{z}} \times \mathbf{u} = -\frac{1}{\rho_0}\nabla_3 p' - \hat{\mathbf{z}}\frac{g\rho'}{\rho_0} + \partial_z(A_v \partial_z \mathbf{u}). \quad \text{(A4)}$$

Note that $p' \ll p$ and $\rho' \ll \rho$. Now project (A4) onto the along-isobath direction $\hat{\mathbf{a}}$,

$$\partial_t v + (\mathbf{u}_3 \cdot \nabla_3 \mathbf{u}) \cdot \hat{\mathbf{a}} + fu = -\frac{1}{\rho_0}\partial_y p' + \partial_z(A_v \partial_z v), \quad \text{(A5)}$$

where u and v are respectively the cross-isobath and along-isobath velocities, y denotes the along-isobath direction and thus $\partial_y p'$ is the along-isobath pressure gradient. The along-isobath direction $\hat{\mathbf{a}}$, which is the direction along the 200-m isobath, varies spatially.

The topographic form stress concept arises from integrating (A5) over a volume $\hat{\mathbf{V}}$. And $\hat{\mathbf{V}}$ here covers the entire horizontal area in our selected region, extending from the bottom to the surface,

$$\int_{\hat{\mathbf{V}}} [\partial_t v + (\mathbf{u}_3 \cdot \nabla_3 \mathbf{u}) \cdot \hat{\mathbf{a}} + fu - \partial_z(A_v \partial_z v)]\, dV = -\frac{1}{\rho_0}\int_{\hat{\mathbf{V}}} \partial_y p'\, dV. \quad \text{(A6)}$$

Assuming $p'(\mathbf{x}, \eta)$ is zero, we can expand the along-isobath pressure gradient term from (A6),

$$\begin{aligned} -\frac{1}{\rho_0}\int_{\hat{\mathbf{V}}} \partial_y p' dV &= -\frac{1}{\rho_0}\int_{\hat{\mathbf{A}}}\int_{z=-h}^{z=\eta} \partial_y p'\, dz\, dA \\ &= \underbrace{-\frac{1}{\rho_0}\int_{\hat{\mathbf{A}}} \partial_y \left(\int_{z=-h}^{z=\eta} p'\, dz\right) dA}_{D_{\mathrm{side},a}} \\ &\quad + \underbrace{\frac{1}{\rho_0}\int_{\hat{\mathbf{A}}} p'(\mathbf{x}, -h)\, h_y\, dA}_{D_{\mathrm{topo},a}}, \end{aligned} \quad \text{(A7)}$$

where $\hat{\mathbf{A}}$ is the horizontal area for the selected CUC region, $\int \cdot\, dA$ the horizontal integral, z the vertical direction, $\int \cdot\, dz$ the vertical integral, h ocean depth, η is SSH, $p'(\mathbf{x}, -h)$ is bottom p', and $D_{\mathrm{topo},a}$ from (A7) represents the along-isobath topographic form stress.

An alternative decomposition of pressure gradient exists. Assuming the ocean is hydrostatic,

$$p(\mathbf{x},z,t) = p_a + \int_z^{\eta} \rho(\mathbf{x},z,t) g\, dz = p_a + \int_z^{\eta} [\hat{\rho}(z,t) + \rho'(\mathbf{x},z,t)] g\, dz, \tag{A8}$$

where p_a is atmospheric pressure at $z = \eta$. Assuming $\rho \approx \rho_0$ at $z = [0, \eta]$ and $\nabla p_a \approx 0$,

$$-\nabla p = -\nabla p' = -g\rho_0 \nabla \eta - g\int_z^0 \nabla \rho'\, dz. \tag{A9}$$

Therefore, the along-isobath pressure gradient volume averaged over $\hat{\mathbf{V}}$ can decomposed as

$$-\frac{1}{\rho_0}\int_{\hat{\mathbf{V}}} \partial_y p'\, dV = \underbrace{-g\int_{\hat{\mathbf{V}}} \partial_y \eta\, dV}_{\mathrm{SSH}_a} + \underbrace{\int_{\hat{\mathbf{V}}} \left(-\frac{g}{\rho_0}\int_z^0 \partial_y \rho'\, dz\right) dV}_{\mathrm{BC}_a}, \tag{A10}$$

where SSH_a and BC_a respectively denote the along-isobath pressure gradient induced by the tilting of SSH or isopycnals in the ocean interior.

A similar rationale leads to the decomposition of cross-isobath pressure gradient,

$$-\frac{1}{\rho_0}\int_{\hat{\mathbf{V}}} \partial_x p'\, dV = \underbrace{-\frac{1}{\rho_0}\int_{\hat{\mathbf{A}}} \partial_x \left(\int_{z=-h}^{z=\eta} p'\, dz\right) dA}_{D_{\mathrm{side},c}} + \underbrace{\frac{1}{\rho_0}\int_{\hat{\mathbf{A}}} p'(\mathbf{x},-h) h_x\, dA}_{D_{\mathrm{topo},c}} \tag{A11}$$

$$= \underbrace{-g\int_{\hat{\mathbf{V}}} \partial_x \eta\, dV}_{\mathrm{SSH}_c} + \underbrace{\int_{\hat{\mathbf{V}}} \left(-\frac{g}{\rho_0}\int_z^0 \partial_x \rho'\, dz\right) dV}_{\mathrm{BC}_c}, \tag{A12}$$

where $D_{\mathrm{topo},c}$ is the cross-isobath topographic form stress. The terms with subscript c hereafter are the same as those with subscript a but for the cross-isobath direction. And we present the volume averaged terms (Figs. 11 and 12).

The term $D_{\mathrm{side},a}$ denotes the pressure acting on the side area of the volume $\hat{\mathbf{V}}$ projected onto the along-isobath direction, and $D_{\mathrm{topo},a}$ is that acting on the bottom of $\hat{\mathbf{V}}$. Following MacCready et al. (2003), assuming the along-isobath direction $\hat{\mathbf{a}}$ varies slowly spatially and thus roughly constant, we can rewrite the volume integrated along-isobath pressure term

$$-\frac{1}{\rho_0}\int_{\hat{\mathbf{V}}} \partial_y p' dV = -\frac{1}{\rho_0}\int_{\hat{\mathbf{V}}} (\nabla_3 p')\cdot \hat{\mathbf{a}}\, dV = -\frac{1}{\rho_0}\int_{\hat{\mathbf{A}}_{\mathrm{SIDE}}} p' \hat{\mathbf{a}}\cdot\hat{\mathbf{n}}\, dA - \frac{1}{\rho_0}\int_{\hat{\mathbf{A}}_{\mathrm{BOT}}} p' \hat{\mathbf{a}}\cdot\hat{\mathbf{n}}\, dA, \tag{A13}$$

where $\hat{\mathbf{A}}_{\mathrm{SIDE}}$ and $\hat{\mathbf{A}}_{\mathrm{BOT}}$ are the side and bottom area enclosing $\hat{\mathbf{V}}$. The last term in (A13) is the topographic form stress for $\hat{\mathbf{V}}$ (MacCready et al. 2003).

Our derivation differs from the conventional formalism. First, topographic form stress is projected onto the spatially varying along-isobath and cross-isobath directions. Second, p' here is the deviation of the total pressure p from the spatially averaged p at a constant depth at each time step [(A2)]. Yet, p' from MacCready et al. (2003) is the deviation of p from the spatially and temporally averaged p at a constant depth, and McCabe et al. (2006) choose p' to be the total pressure. Our choice can reduce the estimation errors of the topographic form stress. Because $\hat{p}(-h, t)$ does not vary horizontally and thus has no dynamical effect in the momentum budget. However, $(1/\rho_0)\int_{\mathbf{A}_0} \hat{p}(-h, t) h_y\, dA$ would be large, unless $\hat{\mathbf{V}}$ is enclosed by topography contours.

APPENDIX B

Eddy-Induced Velocity and Eddy Stress

Here we extend the formalism in Colas et al. (2013) to an expression for the eddy stress divergence $\mathbf{J}$, as a force in the horizontal momentum equation, which is related to eddy buoyancy flux, $(\overline{\mathbf{u}'b'}, \overline{w'b'})$. We hereafter term $\mathbf{J}$ as "eddy force." This approach is similar but not equivalent to two other theoretical frameworks. One is an isopycnal-coordinate eddy-mean decomposition where the averages are made at constant density. The other is the transformed Eulerian mean theory, where the attention is more completely shifted from the Eulerian mean velocity $\overline{\mathbf{u}}_3$ to the residual mean velocity $(\overline{\mathbf{u}}_r, \overline{\mathbf{w}}_r)$ than will be done here.

The goal of our eddy stress analysis is diagnostic. We start from the mean equations,

$$\partial_t \overline{\mathbf{u}} = -\overline{\mathbf{u}_3\cdot\nabla_3 \mathbf{u}} - f\hat{\mathbf{z}}\times\overline{\mathbf{u}} - \frac{1}{\rho_0}\nabla\overline{p} + \partial_z(\overline{A_v \partial_z \mathbf{u}}) + \mathbf{F}_h, \tag{B1}$$

$$\partial_t \overline{b} = -\overline{\mathbf{u}}_3\cdot\nabla_3 \overline{b} - \nabla_3\cdot\overline{\mathbf{u}'_3 b'} + \partial_z(\overline{\kappa_v \partial_z b}) + \overline{D_h}, \tag{B2}$$

where $\mathbf{u}$ is horizontal velocity, f the Coriolis parameter, p pressure, A_v vertical viscosity, κ_v vertical diffusivity, $\mathbf{F}_h$ and D_h horizontal eddy viscosity and diffusion terms, and $\hat{\mathbf{z}}$ is a unit vertical vector. These balances can be evaluated in the conventional way (sections 4 and 5). However, we can reformulate (B1) and (B2) through replacing most eddy flux divergence by a redefined mean advection in the buoyancy balance, and replacing the Coriolis and pressure gradient terms by a residual mean Coriolis force plus the eddy force $\mathbf{J}$ in horizontal momentum. This has the advantage of (i) focusing on the geostrophic mean advection in the buoyancy equation and (ii) providing an eddy force term to compare with other forces in the horizontal momentum equation.

This can be done with the following decomposition: $\overline{\mathbf{u}}_3 = \overline{\mathbf{u}}_g + \overline{\mathbf{u}}_{\mathrm{ag},3}$ and $\overline{\mathbf{u}}_{\mathrm{ag},3} = -\mathbf{u}_{e3} + \overline{\mathbf{u}}_{r3}$. Here the subscripts g, ag, e, and r respectively denote the geostrophic, ageostrophic, eddy-induced, and residual-mean components. This decomposition is motivated by the expectations that the ageostrophic flow is weaker than the geostrophic one, and that the residual

component is no larger than the eddy-induced one. We define $\mathbf{u}_{e3} = \nabla_3 \times \Psi_3$, and its relation to the eddy buoyancy flux is

$$\overline{\mathbf{u}'_3 b'} = \Psi_3 \times \nabla_3 \overline{b} + \mathbf{F}_{e3}\,, \tag{B3}$$

where $\mathbf{F}_{e3}$ is the "turbulent" or "subgrid-scale" or "diabatic" or "diffusive" eddy flux related to subgrid-scale parameterizations (Colas et al. 2013). The along-isopycnal component of $\mathbf{F}_{e3}$ is trivial, although the isopycnal diffusion of other material concentrations can be important (Gent and McWilliams 1990). The diapycnal component of $\mathbf{F}_{e3}$ is generally small outside the turbulent boundary layers.

Assuming that $\mathbf{F}_{e3}$ can be either neglected or diagnosed and subtracted from the eddy fluxes, the eddy-induced streamfunction Ψ_3 can be evaluated from the inversion of (B3):

$$\Psi_3 \approx -(\overline{\mathbf{u}'_3 b'} \times \nabla_3 \overline{b})/|\nabla_3 \overline{b}|^2\,. \tag{B4}$$

Colas et al. (2013) expand these vector relations in their component forms and suggest that a gauge choice can be made for Ψ_3 such that the horizontal component of $\mathbf{u}_e$ has no vertical component of its curl, $\partial_x v_e - \partial_y u_e = 0$. This leads to the gauge condition linking the horizontal component (Ψ) with the vertical component (Ψ^z) of the eddy-induced streamfunction,

$$\nabla^2 \Psi^z = \partial_z \nabla \cdot \Psi\,, \tag{B5}$$

which is unnecessary but helps interpret $\mathbf{u}_e$ and may reduce the magnitude of Ψ_{e3} and $\mathbf{u}_{e3}$.

With the preceding decompositions, (B1) and (B2) are equivalently written as

$$\partial_t \overline{\mathbf{u}} = -f\hat{\mathbf{z}} \times \overline{\mathbf{u}}_r + \mathbf{J} - \overline{\mathbf{u}}_3 \cdot \nabla_3 \overline{\mathbf{u}} + \partial_z(\overline{A_v \partial_z \mathbf{u}}) + \mathbf{F}_h \tag{B6}$$

$$\partial_t \overline{b} = -\overline{\mathbf{u}}_g \cdot \nabla \overline{b} - \overline{\mathbf{u}}_{r3} \cdot \nabla_3 \overline{b} - \nabla_3 \cdot \mathbf{F}_{e3} + \partial_z(\overline{\kappa_v \partial_z b}) + \overline{D_h}\,. \tag{B7}$$

Thus, the geostrophic relation is eliminated, the eddy force J is explicitly present, buoyancy advection is dominated by $\overline{\mathbf{u}}_g$, and the total eddy buoyancy flux divergence is replaced by only the part due to $\mathbf{F}_{e3}$. Subtracting (B6) from (B1) leads to

$$-f\hat{\mathbf{z}} \times \overline{\mathbf{u}}_{\text{ag}} = -f\hat{\mathbf{z}} \times \overline{\mathbf{u}}_r + \mathbf{J}, \tag{B8}$$

where $\mathbf{u}_{\text{ag}}$ is ageostrophic velocity. Equation (B8) indicates that the part of the Coriolis force induced by the mean ageostrophic velocity can be decomposed into the eddy force $\mathbf{J}$ and the Coriolis force induced by the residual mean velocity. The simplifications of the buoyancy balance depend on

$$\mathbf{u}_{e3} \cdot \nabla_3 \overline{b} = \nabla_3 \cdot \overline{\mathbf{u}'_3 b'} + \nabla_3 \cdot \mathbf{F}_{e3}, \tag{B9}$$

and the associated expression for the horizontal eddy stress divergence is

$$\mathbf{J} = f\hat{\mathbf{z}} \times \mathbf{u}_e = f(\nabla \Psi^z - \partial_z \Psi). \tag{B10}$$

Consider the scenario consistent with the adiabatic quasigeostrophic flow: 1) small $\overline{\mathbf{u}}_{r3}$, 2) small $\mathbf{F}_{e3}$, and 3) small isopycnal slope $|\nabla \overline{b}/\partial_z \overline{b}|$. In this case, the only simplification to the preceding general formulas is to express ψ in terms of horizontal eddy fluxes, $\Psi \approx \hat{\mathbf{z}} \times (\overline{\mathbf{u}'b'})/\partial_z \overline{b}$, with Ψ^z determined from (B5). The horizontal eddy stress divergence is thus simply

$$\mathbf{J} = f\hat{\mathbf{z}} \times \mathbf{u}_e = -f\partial_z[\hat{\mathbf{z}} \times (\mathbf{u}'b')/\partial_z \overline{b}] = \partial_z \overline{\tau}_e\,, \tag{B11}$$

where $\overline{\tau}_e$ is the eddy stress, $\overline{\tau}_e = -f\hat{\mathbf{z}} \times \overline{\mathbf{u}'b'}/\partial_z \overline{b}$, and $\mathbf{u}_e$ is the eddy induced velocity,

$$\mathbf{u}_e = -\partial_z(\overline{\mathbf{u}'b'}/\partial_z \overline{b}) \tag{B12}$$

If we further assume that the system is zonally periodic, $\overline{\mathbf{u}}$ is only in the $\hat{\mathbf{x}}$ direction, $\overline{u'b'}$ is ignored, hence (B11) is reduced to the form much discussed in the ACC or atmospheric literature (e.g., Vallis 2016),

$$\mathbf{J} \approx \partial_z [f_0 \overline{v'b'}/\partial_z \overline{b}]\,\hat{\mathbf{x}}\,. \tag{B13}$$

Since the CUC is not zonally periodic, section 7 evaluates eddy stress using (B11) instead of (B13).

APPENDIX C

Relation between Eddy Stress and Isopycnal Form Stress

In horizontally nonuniform regions (e.g., Kuroshio Extension and CUC), eddy stress not only transfers momentum vertically through isopycnal form stress, but also redistributes momentum horizontally. The rationale is as follows. The time-mean isopycnal form stress $\overline{\boldsymbol{\tau}}_d$ is defined as

$$\overline{\tau}_d = \frac{1}{\rho_0}\overline{p'\nabla\eta'} = \frac{1}{\rho_0}\nabla(\overline{p'\eta'}) - \frac{1}{\rho_0}\overline{\eta'\nabla p'}, \tag{C1}$$

where η' is the vertical fluctuation of a certain isopycnal, p' pressure anomaly, and ∇ the horizontal spatial derivative (Ward and Hogg 2011). Because $f\hat{\mathbf{z}} \times \mathbf{u}'_g = -\nabla p'/\rho_0$ and $\eta' \approx -b'/\partial_z \overline{b}$ (Vallis 2016), (C1) can be rewritten as

$$\overline{\tau}_d \approx \frac{1}{\rho_0}\nabla(\overline{p'\eta'}) - f\overline{\hat{\mathbf{z}} \times \mathbf{u}'_g b'/b_z} \approx \frac{1}{\rho_0}\nabla(\overline{p'\eta'}) + \overline{\tau}_e\,. \tag{C2}$$

Therefore, the eddy stress $\overline{\tau}_e$ can be divided into the isopycnal form stress $\overline{\tau}_d$ and the term $\overline{\tau}_{\text{div}}$

$$\overline{\tau}_e \approx \underbrace{\frac{1}{\rho_0}\overline{p'\nabla\eta'}}_{\overline{\tau}_d} - \underbrace{\frac{1}{\rho_0}\nabla(\overline{p'\eta'})}_{\overline{\tau}_{\text{div}}}\,. \tag{C3}$$

The term $\overline{\tau}_{\text{div}}$ involves the correlation between p' and η'. $\overline{\boldsymbol{\tau}}_e$ is equivalent to the isopycnal form stress $\overline{\tau}_d$ only in spatially homogeneous regions, where $\overline{\tau}_{\text{div}}$ is zero.

Combining (5) and (C3) leads to

$$\mathbf{J} \approx \frac{\partial}{\partial z}\overline{\tau}_d - \frac{\partial}{\partial z}\overline{\tau}_{\text{div}} = \frac{\partial}{\partial z}\overline{\tau}_d - \frac{\partial}{\partial z}\left[\frac{1}{\rho_0}\nabla(\overline{p'\eta'})\right]. \tag{C4}$$

The first term of the right-hand side of (C4) represents the vertical transfer of momentum through the isopycnal form stress. The second term acts to redistribute horizontal momentum both vertically and horizontally. Combining Eqs. (B11) and (C3) leads to an expression for eddy-induced velocity

(not shown), which is analogous to Eq. (36) from Greatbatch (1998). However, their Eq. (36) is derived in isopycnal coordinates and thus more complicated.

REFERENCES

Barth, J. A., S. D. Pierce, and T. J. Cowles, 2005: Mesoscale structure and its seasonal evolution in the northern California Current System. *Deep-Sea Res. II*, **52**, 5–28, https://doi.org/10.1016/j.dsr2.2004.09.026.

Becker, J., and Coauthors, 2009: Global bathymetry and elevation data at 30 arc seconds resolution: SRTM30_PLUS. *Mar. Geod.*, **32**, 355–371, https://doi.org/10.1080/01490410903297766.

Bograd, S. J., D. A. Checkley Jr., and W. S. Wooster, 2003: CalCOFI: A half century of physical, chemical, and biological research in the California Current System. *Deep Sea Res. II*, **50**, 2349–2353, https://doi.org/10.1016/S0967-0645(03)00122-X.

Bray, N., A. Keyes, and W. Morawitz, 1999: The California current system in the Southern California Bight and the Santa Barbara Channel. *J. Geophys. Res. Oceans*, **104**, 7695–7714, https://doi.org/10.1029/1998JC900038.

Capet, X., P. Marchesiello, and J. McWilliams, 2004: Upwelling response to coastal wind profiles. *Geophys. Res. Lett.*, **31**, L13311, https://doi.org/10.1029/2004GL020123.

——, J. C. McWilliams, M. J. Molemaker, and A. Shchepetkin, 2008: Mesoscale to submesoscale transition in the California Current System. Part I: Flow structure, eddy flux, and observational tests. *J. Phys. Oceanogr.*, **38**, 29–43, https://doi.org/10.1175/2007JPO3671.1.

Checkley, J. D. M., and J. A. Barth, 2009: Patterns and processes in the California Current System. *Prog. Oceanogr.*, **83**, 49–64, https://doi.org/10.1016/j.pocean.2009.07.028.

Chelton, D. B., 1982: Large-scale response of the California current to forcing by the wind stress curl. CalCOFI Rep., Vol. 23, 30–148, https://www.calcofi.org/publications/calcofireports/v23/CalCOFI_Rpt_Vol_23_1982.pdf.

——, 1984: Seasonal variability of alongshore geostrophic velocity off central California. *J. Geophys. Res.*, **89**, 3473–3486, https://doi.org/10.1029/JC089iC03p03473.

Chen, R., A. F. Thompson, and G. R. Flierl, 2016: Time-dependent eddy-mean energy diagrams and their application to the ocean. *J. Phys. Oceanogr.*, **46**, 2827–2850, https://doi.org/10.1175/JPO-D-16-0012.1.

Chenillat, F., P. J. Franks, X. Capet, P. Rivière, N. Grima, B. Blanke, and V. Combes, 2018: Eddy properties in the Southern California Current System. *Ocean Dyn.*, **68**, 761–777, https://doi.org/10.1007/s10236-018-1158-4.

Colas, F., X. Capet, J. C. McWilliams, and Z. Li, 2013: Mesoscale eddy buoyancy flux and eddy-induced circulation in eastern boundary currents. *J. Phys. Oceanogr.*, **43**, 1073–1095, https://doi.org/10.1175/JPO-D-11-0241.1.

Collins, C., R. Paquette, and S. Ramp, 1996: Annual variability of ocean currents at 350-m depth over the continental slope off Point Sur, California. CalCOFI Rep., Vol. 37, 257–263, http://www.calcofi.org/publications/calcofireports/v37/Vol_37_Collins_etal.pdf.

Collins, C. A., L. M. Ivanov, O. V. Melnichenko, and N. Garfield, 2004: California Undercurrent variability and eddy transport estimated from RAFOS float observations. *J. Geophys. Res.*, **109**, C05028, https://doi.org/10.1029/2003JC002191.

——, T. Margolina, T. A. Rago, and L. Ivanov, 2013: Looping RAFOS floats in the California Current System. *Deep-Sea Res. II*, **85**, 42–61, https://doi.org/10.1016/j.dsr2.2012.07.027.

Connolly, T. P., B. M. Hickey, I. Shulman, and R. E. Thomson, 2014: Coastal trapped waves, alongshore pressure gradients, and the California Undercurrent. *J. Phys. Oceanogr.*, **44**, 319–342, https://doi.org/10.1175/JPO-D-13-095.1.

Cornuelle, B., T. Chereskin, P. Niiler, M. Morris, and D. Musgrave, 2000: Observations and modeling of a California Undercurrent eddy. *J. Geophys. Res.*, **105**, 1227–1243, https://doi.org/10.1029/1999JC900284.

Danabasoglu, G., J. C. McWilliams, and P. R. Gent, 1994: The role of mesoscale tracer transports in the global ocean circulation. *Science*, **264**, 1123–1126, https://doi.org/10.1126/science.264.5162.1123.

Duran, R., 2019: Kinematics and dynamics of a model eastern-boundary poleward undercurrent. Ph.D. thesis, Oregon State University, 179 pp.

Ferreira, D., J. Marshall, and P. Heimbach, 2005: Estimating eddy stresses by fitting dynamics to observations using a residual-mean ocean circulation model and its adjoint. *J. Phys. Oceanogr.*, **35**, 1891–1910, https://doi.org/10.1175/JPO2785.1.

Frischknecht, M., M. Münnich, and N. Gruber, 2015: Remote versus local influence of ENSO on the California Current System. *J. Geophys. Res. Oceans*, **120**, 1353–1374, https://doi.org/10.1002/2014JC010531.

Garfield, N., C. A. Collins, R. G. Paquette, and E. Carter, 1999: Lagrangian exploration of the California Undercurrent, 1992–95. *J. Phys. Oceanogr.*, **29**, 560–583, https://doi.org/10.1175/1520-0485(1999)029<0560:LEOTCU>2.0.CO;2.

Gay, P. S., and T. K. Chereskin, 2009: Mean structure and seasonal variability of the poleward undercurrent off Southern California. *J. Geophys. Res.*, **114**, C02007, https://doi.org/10.1029/2008JC004886.

Gent, P. R., and J. C. McWilliams, 1990: Isopycnal mixing in ocean circulation models. *J. Phys. Oceanogr.*, **20**, 150–155, https://doi.org/10.1175/1520-0485(1990)020<0150:IMIOCM>2.0.CO;2.

Gómez-Valdivia, F., A. Parés-Sierra, and A. L. Flores-Morales, 2017: Semiannual variability of the California Undercurrent along the Southern California Current System: A tropical generated phenomenon. *J. Geophys. Res. Oceans*, **122**, 1574–1589, https://doi.org/10.1002/2016JC012350.

Greatbatch, R. J., 1998: Exploring the relationship between eddy-induced transport velocity, vertical momentum transfer, and the isopycnal flux of potential vorticity. *J. Phys. Oceanogr.*, **28**, 422–432, https://doi.org/10.1175/1520-0485(1998)028<0422:ETRBEI>2.0.CO;2.

Halo, I., P. Penven, B. Backeberg, I. Ansorge, F. Shillington, and R. Roman, 2014: Mesoscale eddy variability in the southern extension of the East Madagascar Current: Seasonal cycle, energy conversion terms, and eddy mean properties. *J. Geophys. Res. Oceans*, **119**, 7324–7356, https://doi.org/10.1002/2014JC009820.

Hickey, B. M., 1979: The California Current System-hypotheses and facts. *Prog. Oceanogr.*, **8**, 191–279, https://doi.org/10.1016/0079-6611(79)90002-8.

——, and N. E. Pola, 1983: The seasonal alongshore pressure gradient on the west coast of the United States. *J. Geophys. Res.*, **88**, 7623–7633, https://doi.org/10.1029/JC088iC12p07623.

Hill, A. E., B. M. Hickey, F. A. Shillington, P. T. Strub, K. H. Brink, E. D. Barton, and A. C. Thomas, 1998: Eastern ocean boundaries. *The Global Coastal Ocean: Regional Studies and Syntheses*, A. R. Robinson and K. H. Brink, Eds., *The Sea—Ideas and Observations on Progress in the Study of the Seas*, Vol. 11, John Wiley and Sons, 29–67.

Holloway, G., 1987: Systematic forcing of large-scale geophysical flows by eddy-topography interaction. *J. Fluid Mech.*, **184**, 463–476, https://doi.org/10.1017/S0022112087002970.

——, 1992: Representing topographic stress for large-scale ocean models. *J. Phys. Oceanogr.*, **22**, 1033–1046, https://doi.org/10.1175/1520-0485(1992)022<1033:RTSFLS>2.0.CO;2.

——, 1996: Neptune effect: Statistical mechanical forcing of ocean circulation. *Stochastic Modelling in Physical Oceanography*, Springer, 207–219.

——, and Z. Wang, 2009: Representing eddy stress in an Arctic Ocean model. *J. Geophys. Res. Oceans*, **114**, C06020, https://doi.org/10.1029/2008JC005169.

Hurlburt, H., and J. D. Thompson, 1973: Coastal upwelling on a β-plane. *J. Phys. Oceanogr.*, **3**, 16–32, https://doi.org/10.1175/1520-0485(1973)003<0016:CUOAP>2.0.CO;2.

Klymak, J. M., 2018: Nonpropagating form drag and turbulence due to stratified flow over large-scale abyssal hill topography. *J. Phys. Oceanogr.*, **48**, 2383–2395, https://doi.org/10.1175/JPO-D-17-0225.1.

Large, W. G., J. C. McWilliams, and S. C. Doney, 1994: Oceanic vertical mixing: A review and a model with nonlocal boundary layer parameterization. *Rev. Geophys.*, **32**, 363–403, https://doi.org/10.1029/94RG01872.

Lynn, R. J., and J. J. Simpson, 1987: The California Current System: The seasonal variability of its physical characteristics. *J. Geophys. Res.*, **92**, 12 947–12 966, https://doi.org/10.1029/JC092iC12p12947.

MacCready, P., G. Pawlak, K. Edwards, and R. McCabe, 2003: Form drag on ocean flows. *Near Boundary Processes and Their Parameterization: Proc. 13th'Aha Huliko'a Hawaiian Winter Workshop*, Honolulu, HI, University of Hawai'i at Mānoa, 119–130.

Maltrud, M., and G. Holloway, 2008: Implementing biharmonic Neptune in a global eddying ocean model. *Ocean Modell.*, **21**, 22–34, https://doi.org/10.1016/j.ocemod.2007.11.003.

Marchesiello, P., J. C. McWilliams, and A. Shchepetkin, 2003: Equilibrium structure and dynamics of the California Current system. *J. Phys. Oceanogr.*, **33**, 753–783, https://doi.org/10.1175/1520-0485(2003)33<753:ESADOT>2.0.CO;2.

McCabe, R. M., P. MacCready, and G. Pawlak, 2006: Form drag due to flow separation at a headland. *J. Phys. Oceanogr.*, **36**, 2136–2152, https://doi.org/10.1175/JPO2966.1.

McCreary, J. P., 1981: A linear stratified ocean model of the coastal undercurrent. *Philos. Trans. Roy. Soc. London*, **302A**, 385–413, https://doi.org/10.1098/rsta.1981.0176.

——, P. K. Kundu, and S.-Y. Chao, 1987: On the dynamics of the California Current System. *J. Mar. Res.*, **45**, 1–32, https://doi.org/10.1357/002224087788400945.

McWilliams, J. C., W. R. Holland, and J. H. Chow, 1978: A description of numerical Antarctic Circumpolar Currents. *Dyn. Atmos. Oceans*, **2**, 213–291, https://doi.org/10.1016/0377-0265(78)90018-0.

Meinvielle, M., and G. C. Johnson, 2013: Decadal water-property trends in the California Undercurrent, with implications for ocean acidification. *J. Geophys. Res. Oceans*, **118**, 6687–6703, https://doi.org/10.1002/2013JC009299.

Molemaker, M. J., J. C. McWilliams, and W. K. Dewar, 2015: Submesoscale instability and generation of mesoscale anticyclones near a separation of the California Undercurrent. *J. Phys. Oceanogr.*, **45**, 613–629, https://doi.org/10.1175/JPO-D-13-0225.1.

Naveira Garabato, A. C., A. G. Nurser, R. B. Scott, and J. A. Goff, 2013: The impact of small-scale topography on the dynamical balance of the ocean. *J. Phys. Oceanogr.*, **43**, 647–668, https://doi.org/10.1175/JPO-D-12-056.1.

Penduff, T., B. Barnier, M.-A. Kerbiriou, and J. Verron, 2002: How topographic smoothing contributes to differences between the eddy flows simulated by sigma-and geopotential-coordinate models. *J. Phys. Oceanogr.*, **32**, 122–137, https://doi.org/10.1175/1520-0485(2002)032<0122:HTSCTD>2.0.CO;2.

Pierce, S., R. Smith, P. Kosro, J. Barth, and C. Wilson, 2000: Continuity of the poleward undercurrent along the eastern boundary of the mid-latitude north Pacific. *Deep-Sea Res. II*, **47**, 811–829, https://doi.org/10.1016/S0967-0645(99)00128-9.

Reid, J., 1962: Measurements of the California Countercurrent at a depth of 250 meters. *J. Mar. Res.*, **20**, 134–137.

Renault, L., C. Deutsch, J. C. McWilliams, H. Frenzel, J.-H. Liang, and F. Colas, 2016a: Partial decoupling of primary productivity from upwelling in the California Current system. *Nat. Geosci.*, **9**, 505–508, https://doi.org/10.1038/ngeo2722.

——, A. Hall, and J. C. McWilliams, 2016b: Orographic shaping of US West Coast wind profiles during the upwelling season. *Climate Dyn.*, **46**, 273–289, https://doi.org/10.1007/s00382-015-2583-4.

——, M. J. Molemaker, J. C. McWilliams, A. F. Shchepetkin, F. Lemarié, D. Chelton, S. Illig, and A. Hall, 2016c: Modulation of wind work by oceanic current interaction with the atmosphere. *J. Phys. Oceanogr.*, **46**, 1685–1704, https://doi.org/10.1175/JPO-D-15-0232.1.

——, S. Masson, T. Arsouze, G. Madec, and J. C. McWilliams, 2020: Recipes for how to force oceanic model dynamics. *J. Adv. Model. Earth Syst.*, **12**, e2019MS001715, https://doi.org/10.1029/2019MS001715.

——, J. C. McWilliams, F. Kessouri, A. Jousse, H. Frenzel, R. Chen, and C. Deutsch, 2021: Evaluation of high-resolution atmospheric and oceanic simulations of the California Current System. *Prog. Oceanogr.*, **195**, 102564, https://doi.org/10.1016/j.pocean.2021.102564.

Salmon, R., 1998: Linear ocean circulation theory with realistic bathymetry. *J. Mar. Res.*, **56**, 833–884, https://doi.org/10.1357/002224098321667396.

Samelson, R., 2017: Time-dependent linear theory for the generation of poleward undercurrents on eastern boundaries. *J. Phys. Oceanogr.*, **47**, 3037–3059, https://doi.org/10.1175/JPO-D-17-0077.1.

Shchepetkin, A. F., and J. C. McWilliams, 2005: The regional oceanic modeling system (ROMS): A split-explicit, free-surface, topography-following-coordinate oceanic model. *Ocean Modell.*, **9**, 347–404, https://doi.org/10.1016/j.ocemod.2004.08.002.

——, and ——, 2009: Correction and commentary for "Ocean forecasting in terrain-following coordinates: Formulation and skill assessment of the regional ocean modeling system" by Haidvogel et al., J. Comp. Phys. 227, pp. 3595–3624. *J. Comput. Phys.*, **228**, 8985–9000, https://doi.org/10.1016/j.jcp.2009.09.002.

Skamarock, W. C., and Coauthors, 2008: A description of the Advanced Research WRF version 3. NCAR Tech. Note NCAR/TN-475+STR, 113 pp., https://doi.org/10.5065/D68S4MVH.

Stewart, A., and A. Thompson, 2016: Eddy generation and jet formation via dense water outflows across the Antarctic continental slope. *J. Phys. Oceanogr.*, **46**, 3729–3750, https://doi.org/10.1175/JPO-D-16-0145.1.

Storch, J.-S., C. Eden, I. Fast, H. Haak, D. Hernández-Deckers, E. Maier-Reimer, J. Marotzke, and D. Stammer, 2012: An estimate of the Lorenz energy cycle for the world ocean based on the STORM/NCEP simulation. *J. Phys. Oceanogr.*, **42**, 2185–2205, https://doi.org/10.1175/JPO-D-12-079.1.

Thomson, R. E., and M. V. Krassovski, 2010: Poleward reach of the California Undercurrent extension. *J. Geophys. Res.*, **115**, C09027, https://doi.org/10.1029/2010JC006280.

——, and ——, 2015: Remote alongshore winds drive variability of the California Undercurrent off the British Columbia-Washington coast. *J. Geophys. Res. Oceans*, **120**, 8151–8176, https://doi.org/10.1002/2015JC011306.

Todd, R. E., D. L. Rudnick, R. E. Davis, and M. D. Ohman, 2011: Underwater gliders reveal rapid arrival of El Niño effects off California's coast. *Geophys. Res. Lett.*, **38**, L03609, https://doi.org/10.1029/2010GL046376.

Tréguier, A.-M., and J. McWilliams, 1990: Topographic influences on wind-driven, stratified flow in a β-plane channel: An idealized model for the Antarctic Circumpolar Current. *J. Phys. Oceanogr.*, **20**, 321–343, https://doi.org/10.1175/1520-0485(1990)020<0321:TIOWDS>2.0.CO;2.

Tsuchiya, M., 1980: Inshore circulation in the southern California Bight, 1974–1977. *Deep-Sea Res.*, **27A**, 99–118, https://doi.org/10.1016/0198-0149(80)90090-4.

Vallis, G. K., 2016: *Atmospheric and Oceanic Fluid Dynamics*. Cambridge University Press, 745 pp.

Wang, Y., and A. L. Stewart, 2018: Eddy dynamics over continental slopes under retrograde winds: Insights from a model intercomparison. *Ocean Modell.*, **121**, 1–18, https://doi.org/10.1016/j.ocemod.2017.11.006.

Ward, M. L., and A. M. Hogg, 2011: Establishment of momentum balance by form stress in a wind-driven channel. *Ocean Modell.*, **40**, 133–146, https://doi.org/10.1016/j.ocemod.2011.08.004.

Werner, F. E., and B. M. Hickey, 1983: The role of alongshore pressure gradient in Pacific Northwest coastal dynamics. *J. Phys. Oceanogr.*, **13**, 395–410, https://doi.org/10.1175/1520-0485(1983)013<0395:TROALP>2.0.CO;2.

Wolff, J.-O., E. Maier-Reimer, and D. J. Olbers, 1991: Wind-driven flow over topography in a zonal β-plane channel: A quasi-geostrophic model of the Antarctic Circumpolar Current. *J. Phys. Oceanogr.*, **21**, 236–264, https://doi.org/10.1175/1520-0485(1991)021<0236:WDFOTI>2.0.CO;2.

Wooster, W. S., 1970: California undercurrent off northern Baja California. *J. Mar. Res.*, **28**, 235–250.

Wunsch, C., 1998: The work done by the wind on the oceanic general circulation. *J. Phys. Oceanogr.*, **28**, 2332–2340, https://doi.org/10.1175/1520-0485(1998)028<2332:TWDBTW>2.0.CO;2.

Zhai, X., and D. P. Marshall, 2013: Vertical eddy energy fluxes in the North Atlantic subtropical and subpolar gyres. *J. Phys. Oceanogr.*, **43**, 95–103, https://doi.org/10.1175/JPO-D-12-021.1.

Zhan, P., A. C. Subramanian, F. Yao, A. R. Kartadikaria, D. Guo, and I. Hoteit, 2016: The eddy kinetic energy budget in the Red Sea. *J. Geophys. Res. Oceans*, **121**, 4732–4747, https://doi.org/10.1002/2015JC011589.